Making a Superbolt: Reconciling Observations of the Optically Brightest Lightning on Earth from Different Satellites

Michael Peterson[1]

[1]ISR-2, Los Alamos National Laboratory, Los Alamos, New Mexico

Corresponding author: Michael Peterson (mpeterson@lanl.gov), B241, P.O. Box 1663 Los Alamos, NM, 87545

Key Points:

- The top FORTE PDD, LIS, and GLM detections capture different portions of the population of the top optical lightning events
- These differences arise from nuances in the design and operation of these sensors that introduce detection biases
- The FORTE superbolt distribution only represents a subset of all superbolts, which should also include the top LIS / GLM events

LA-UR-23-24435

Abstract

We previously documented geographic distributions of the optically brightest lightning on Earth – known as "superbolts" – using two space-based instruments: the photodiode detector (PDD) on the Fast On-orbit Recording of Transient Events (FORTE) satellite and the Geostationary Lightning Mapper (GLM) on NOAA's newest Geostationary Operational Environmental Satellites (GOES). In this study, we further examine the superbolts identified by the PDD and GLM to reconcile the differences between their geographic distributions. We find that both the physical extent of the parent flash and the development speed of its leaders are important for making a superbolt.

The oceanic PDD superbolts tend to occur early in flashes that rapidly expand laterally into long-horizontal "megaflashes." The top GLM superbolts occur over land at later times in particularly large megaflashes that grow more slowly until they extend over multiple hundreds of kilometers. The FORTE PDD missed these delayed superbolts due to limitations in its triggering.

Coincident TRMM measurements show that the warm season megaflash superbolts detected by LIS/GLM and Turman's (1977) wintertime oceanic superbolts also observed by the PDD occur in otherwise similar thunderstorm environments. Both are marked by: low storm heights (< 10 km), widespread rainfall near the surface, small infrared brightness temperature gradients, and low flash rates. We suggest that the vertically-compact, stratiform nature of these clouds allows them to store more charge between flashes, providing favorable conditions for superbolt production.

Plain Language Summary

The brightest optical pulses from lightning seen from space have been termed "superbolts." Superbolts are incredibly rare, and represent flashes of light that are at least 100 times brighter than what we typically see from lightning. Curiously, the locations and times associated with these brightest optical pulses differ based on the instrument and satellite used. Previous assessments with the Vela satellites and the photodiode detector (PDD) on the FORTE satellite identify wintertime lightning around Japan, along the Gulf Stream in the Atlantic Ocean, and in the Mediterranean Sea as superbolt hotspots. However, assessments with NOAA's Geostationary Lightning Mapper (GLM) find hotspots in regions with large-horizontal "megaflashes"– particularly, the La Plata basin in south America and the south-central Great Plains in the United States.

In this study, we examine how these differences in optical superbolt detections arise. We find that the differing global distributions can be explained by the FORTE PDD missing superbolts that occur late in the flash due to its finite trigger count limit – an issue not encountered by GLM.

1 Introduction

Lightning is a spectacular, yet common, atmospheric phenomenon that impacts life on Earth, sometimes with tragic consequences. With ~44 flashes occurring every second (Christian et al., 2003) and modern lightning detection systems capable of resolving a significant fraction of the flashes within their measurement domains, the lightning research community has been able to document how lightning typically behaves rather well. We know that most lightning is small compared to the size of its parent thunderstorm (on the order of 10 km) while usually occurring entirely within the cloud. Only a fraction of lightning flashes strike the ground, and this subset of Cloud-to-Ground (CG) lightning tends to be of negative polarity with peak currents on the order of 10 kA. We also know that most lightning occurs over land within the convective cores of thunderstorms, where trends in flash rates and flash characteristics provide insights into updraft behavior (Deierling and Petersen, 2008) that can even give advance warning of severe weather (Schultz et al., 2009; Gatlin and Goodman, 2010).

1.1 Exceptional lightning

However, not all lightning fits this “typical” view. Some CG strokes are of a positive polarity with long-lasting Continuing Current (CC) (Mazur, 2002) and peak currents that can reach hundreds of kiloamps (Said et al., 2013). This type of +CG stroke is common in the ~10% (Peterson and Liu, 2011) of lightning that occurs outside of the convective core and propagates through the clouds adjacent to convection (Lang et al., 2004; Carey et al., 2005; Ely et al., 2008). Lightning might not be expected to occur in these regions, but when it does happen, it tends to develop horizontally over considerable distances while initiating multiple CGs along its path (Peterson and Stano, 2021). The largest of these long horizontal flashes have been termed “megaflashes” (Lyons et al., 2020), and they are known to strike “out of the grey” from over the horizon in regions where no lightning had been observed in the prior 30 minutes or more. Thus, typical lightning safety guidance (either the "30-30" rule or NOAA's "when thunder roars, go indoors") would not ensure safety from this exceptional type of lightning.

It is important to document extreme lightning because it challenges our assumptions surrounding the capabilities of lightning, and can guide the development of improved standards for mitigating lightning hazards. Aside from megaflashes, another type of extreme lightning that has received considerable attention recently is the "superbolt." Superbolts are extraordinarily-powerful flashes of light that are produced by certain types of lightning. Superbolts were first detected by the optical payload on the Vela satellites. Turman (1977) reported a distinct class of lightning emissions in the Vela optical data whose peak broadband optical power at the source would have been at least 10^{11} W to even greater than 1 TW. These pulses are 100x brighter than what we consider "normal" lightning with total optical energies integrated through the waveform reaching 10^9 J at the source.

Tuman (1977) also found that these superbolts were not ubiquitous across the lightning-producing regions of the Earth (Christian et al., 2003; Albrecht et al., 2016; Peterson et al., 2020), but rather clustered in regions and seasons where lightning is uncommon – for example winter thunderstorms in the oceans surrounding Japan that are known to have vertically compact precipitation structures (Yamamoto et al., 2006) and for generating +CG strokes (Miyake et al., 1992) that are sufficiently powerful to initiate sprites (Hayakawa et al., 2004). This suggests that superbolts are more than simply the tail of the normal lightning distribution, but instead that they require a specific set of conditions within the storm environment that is generally not met elsewhere.

1.2 When normal lightning appears exceptional

However, it is also possible for normal lightning to appear very optically bright – even to the point of masquerading as a superbolt – if the satellite happens to view it unobscured by the clouds. Most lightning occurs embedded entirely within its parent thunderstorm where the surrounding clouds broaden its optical pulses in space and time through multiple scattering (Light et a., 2001; Thomson et al., 1982; Koshak et al., 1994; Peterson, 2020a; Brunner et al., 2020). The peak optical powers of the signals that transmit through the cloud to space are less intense than the source waveform because much of that energy is scattered away from the satellite, absorbed in the cloud, or delayed into a long tail after traversing longer path lengths through the cloud to the instrument. If that same optical pulse could be viewed with little-to-no cloud between the source and satellite, then the signal would retain its full power.

While lightning flashes only infrequency leave the cloud entirely to be observed as a completely unobscured lightning channel by any satellite in view (for example, to strike the ground as a "bolt from the blue") we can similarly reduce the radiative transfer effects of the clouds by viewing the thunderstorm from the side. Moving the sensor from a nadir view towards a limb view allows it to resolve optical emissions that originate below the overhanging anvil clouds that are known to block optical transmission (Peterson, 2021a), or potentially even below the cloud base. We used a radiative transfer model to simulate this scenario and found that the total radiance from the pulse increased by two orders of magnitude between the source being obscured and unobscured by the cloud (Peterson, 2020a). This roughly agrees with Turman's observation that superbolts are 100x more powerful than normal lightning. The high orbital altitude of the Vela satellites (118,000 km), which was beyond even geostationary orbit (35,000 km), would have provided ample opportunities to observe optical events close to the limb with a near side-view of the storm. Lightning pulses that only reach the superbolt threshold due to instrument viewing angle (and would not be classified as a superbolt by another satellite located elsewhere) would not merit distinction as a special type of lightning phenomenon.

1.3 Modern superbolt detections

Fortunately, multiple instruments have been used to corroborate and expand upon Turman's (1977) superbolt findings. The closest analog to Turman's work are the studies by Kirkland (1999) and Peterson and Kirkland (2020). These two studies leveraged broadband optical measurements from the photodiode detector on the FORTE satellite (Kirkland et al., 2001) to identify superbolts according to their peak optical power estimated at the source. The Low Earth Orbit (LEO) of the FORTE satellite and limited Field of View (FOV) of its PDD instrument mitigate the low elevation angle issue, but also limit the amount of time spent observing thunderstorms in the Earth's superbolt hotspot regions. Still, the FORTE PDD reported more than ten thousand 100-GW superbolts and multiple terawatt-class superbolts during its 12 years of operation between late 1997 and 2010. The more intense superbolt cases (> 350 GW) showed the same wintertime and Sea of Japan / Pacific Ocean clustering noted by Turman (1977), and we were able to confirm the intense +CG origin suggested by Turman (1977) in cases over North America using coincident National Lightning Detection Network (NLDN: Cummins and Murphy, 2009) observations.

We also used optical Geostationary Lightning Mapper (GLM: Goodman et al., 2013; Rudlosky et al., 2019) data from NOAA's current Geostationary Operational Environmental Satellites (GOES-16) to document the most energetic optical pulses in the Americas. Unlike the Vela optical payload or the FORTE PDD that report broadband optical waveforms, GLM reports narrowband (777.4 nm) measurements of the total optical energy received over a 2-ms integration frame. The top GLM lightning pulses are expected to differ somewhat from the top

Vela / PDD events. For example, optical sources that lack the peak power of a superbolt may be able to generate an equivalent total optical energy by persisting over a long duration. Still, the FORTE PDD data show that total optical energy correlates with peak optical power, meaning that the most exceptional events from a total energy perspective are largely still be exceptional from a peak power perspective. Moreover, GLM has a key advantage over FORTE with its geostationary orbit. Continuous staring measurements over the Americas and the adjacent oceans allow GLM to observe even the rarest optical lightning phenomena. Indeed, we found that the most energetic GLM detections frequently occurred in megaflashes in the Great Plains in North America and the La Plata basin in South America (Peterson and Lay, 2020) – regions that were unremarkable in the PDD superbolt distributions due to the difficulty of capturing extreme megaflashes in LEO snapshots.

1.4 Can superbolts be identified using Radio Frequency (RF) data?

Finally, there is the case of the most energetic World-Wide Lightning Location Network (WWLLN: Hutchins et al., 2012; Jacobson and Holzworth, 2006) detections that were described as “superbolts” by Holzworth et al. (2019). Their justification for applying the term “superbolt” to the top Very Low Frequency (VLF) RF events in the WWLLN data was that there is a similar pattern of occurrence to Turman (1977)’s superbolts. However, is it not clear whether these cases actually represent the same lightning phenomena, as no effort was made to link the top WWLLN events with extraordinary optical emissions. The phenomenological differences between RF and optical emission and WWLLN’s poor sensitivity to the in-cloud currents that the optical platforms preferentially detect lead us to suspect that this agreement is may at least partially be coincidental. Evidence to support this idea can be found in the WWLLN maps of top (2 GJ) events shown in Holzworth et al. (2019) where the primary Americas hotspot is along the Andes mountains – an area that certainly produces energetic lightning, but not a hotspot for the most extraordinary optical emissions detected by GLM or the FORTE PDD. Until the link with exceptional optical emission has been established, we will consider these top RF events separately from optical superbolts and not examine them in this study.

1.5 Where are the Earth's top superbolts?

Our two optical space-based sensors – the FORTE PDD and GLM - differ in where and under what environmental conditions they detect their most intense optical lightning events. The challenge with documenting the most extreme lightning on Earth is that these events push the limits of what our instruments were designed to detect. It is unclear to what extent these differences are physical or due to the limitations in our detection technology. In this study, we take a closer look at optical superbolts, their physical development over time, and the thunderstorm environments in which they arise to improve our understanding of how they occur and reconcile the differences between the PDD and GLM maps of the Earth's most extraordinary optical lightning events.

2 Data and Methodology

2.1 The FORTE photodiode detector (PDD)

The FORTE PDD was a silicone photodiode detector that measured broadband (400 nm – 1100 nm) optical waveforms from transient lightning events (Kirkland et al., 2001; Suszcynsky et al., 2000). Its high sampling rate yielded a sufficiently fine temporal resolution (15 μs) to characterize the peak optical power of individual lightning pulses that originated from anywhere within the ~1200 km ground footprint of its 80° circular FOV. PDD records typically contained 1.92 ms of data when the instrument was operating in its primary autonomous mode.

In this mode, the instrument would trigger once the background-compensated signal amplitude exceeded a selected threshold for a commanded number of consecutive samples (usually 5, corresponding to 75 μs). This filter was necessary to prevent artifacts from energetic particle impacts from triggering the instrument. Energetic particle impacts are a significant problem for spacecraft in Low Earth Orbit (LEO), especially as they pass through the South Atlantic Anomaly (SAA) where the Earth's inner Van Allen belts extend to a low altitude. Energetic particles hitting the PDD cause quick 1-2 sample spikes in the waveform that are unlike the comparably slow rises and falls in the light curves from natural lightning (especially after scattering in the cloud medium). Without the consecutive sample filter, the PDD data would consist of mostly artifacts with a high concentration of events in the SAA region that includes much of South America and the southern Atlantic Ocean.

In addition to the energetic particle filter, the PDD was also subject to two limitations on its trigger rate. The first was a minimum intertrigger delay, which was nominally 4.4 ms for its autonomous mode (Suszcynsky et al., 2000). This means that each 1.92 ms record would be followed by a 2.5 ms period of dead time before the next possible trigger. Then, the second was a maximum trigger rate to conserve onboard memory. Once a commanded number of triggers was reached (often 10) during a short time period (often 40 ms), then the PDD would stop triggering until the next GPS-conditioned pulse-per-second signal (Kirkland et al., 2001).

These restrictions on the types of signals that triggered the FORTE PDD and their allowed trigger rates could potentially prevent the PDD from detecting certain kinds of superbolts. The minimum 75 μs pulse width could limit the ability of the PDD to detect near-impulsive lightning emissions from sources that are not obscured by clouds. Moreover, the maximum trigger rate limitation is known to have prevented detections of events that occurred later in lightning flashes (Peterson, 2020a,b). As capable as the PDD was at detecting global lightning, its engineering constrains prevented it from fully resolving the optical emissions from some of the most interesting flashes in nature.

2.2 The Lightning Imaging Sensor (LIS) and Geostationary Lightning Mapper (GLM)

LIS (Christian et al., 2000; Blakeslee et al., 2020) and GLM (Goodman et al., 2013; Rudlosky et al,. 2019) are lightning imagers operated by NASA and NOAA, respectively. Both instruments record the Earth at a nominal frame rate of 500 FPS in a narrow spectral band around the 777.4 nm Oxygen emission line triplet and trigger on transient changes in cloud illumination that are indicative of lightning activity. LIS has been deployed twice in Low Earth Orbit, each time providing lightning snapshots from thunderstorms across the globe: first, on the Tropical Rainfall Measuring Mission (TRMM: 1998 - 2015) satellite, and then on the International Space Station (2017-present). We will only use TRMM-LIS detections in this study to take advantage of the coincident cloud measurements provided by the other TRMM instruments described below. Meanwhile, GLM observes the Americas and the Atlantic and Pacific oceans from the GOES-16 and GOES-17 satellites in geostationary orbit. The public data record for GLM extends back to late 2017 for GOES-16 and 2019 for GOES-17.

LIS and GLM data are comprised of pixel detections where the instantaneous energy received by the instrument exceeds the background illumination by an instrument threshold. These "events" represent illuminated pixels, not complete lightning processes. Thus, they are clustered into more complex features by algorithms described in Mach et al. (2007) and Goodman et al. (2010). “Group” features aggregate all contiguous events on the imaging array within the same integration frame and approximate individual lightning pulses, while “flash” features aggregate groups in close spatiotemporal proximity and approximate distinct lightning flashes. We also have defined an intermediate “series” feature that approximates sustained lightning processes that last longer than an integration frame but shorter than a flash (Peterson and Rudlosky, 2019).

The flash cluster data generated for LIS and GLM provides additional context on how individual optical pulses relate to the larger evolution of the flash. We have used this data to measure the lateral development of lightning flashes (Peterson et al., 2018), to identify the largest and longest-lasting flashes found in nature (Peterson et al., 2020) and document where and when they occur (Peterson, 2021b), and to examine how the surrounding cloud medium is illuminated by lightning (Peterson, 2019a). After correcting the data for degradation due to processing limitations (Peterson, 2019b), the LIS and GLM datasets are particularly well-suited for documenting the diverse collection of lightning that we can observe from space – including the long-lasting flashes that are known to be missed by the PDD.

However, these lightning imagers cannot identify superbolts based on peak power. Their 500 ms nominal frame rates limit their detections to 2-ms integrations of total energy. A whole PDD waveform could be captured in a single LIS or GLM integration frame. Additionally, LIS and GLM are narrowband instruments centered at 777.4 nm, while the PDD was a broadband instrument. The fraction of the broadband optical energy at 777.4 nm in space-based observations is thought to be on the order of 1%, with a value of 4% between the PDD and lightning imager on FORTE reported by Suszcynsky et al. (2001).

All of these factors – delay in the flash, energy versus power, and the spectral content of the signals – plus the different orbits of the parent spacecraft for the PDD, LIS, and GLM may contribute to the differences that we see between their maps of optical superbolts.

2.2.1 Removing Solar Artifacts in the GLM Data

Solar artifacts arise when sunlight can either reflect off a cloud or body of water to reach the optical sensor or intrude directly into the instrument optics. If the reflection is sufficiently impulsive, it might cause the optical instrument to trigger. Solar artifacts are not a severe issue for the two instruments in LEO (the FORTE PDD and LIS) due in large part to their onboard filtering. However, solar artifacts are frequently observed across large swaths of the GLM domain and are sufficiently bright to pose an issue for identifying the superbolts.

We have some methods for removing this glint from the GLM dataset (Peterson, 2020b), but they do not completely mitigate the problem for superbolt cases. For this reason, we take a different approach to solar artifact filtering here. Since we are looking at the peak of the GLM lightning distribution, the ground-based lightning detection networks should be able to detect virtually all of these events. For each of the most energetic GLM groups, we seek a match with a

WWLLN stroke within 16.5 km and 330 ms (the GLM clustering thresholds). If no match is found, then the group is discarded as a potential solar artifact.

2.2.2 Coincident Thunderstorm Measurements for LIS on the TRMM Satellite

While GLM benefits from the continuous monitoring of the near-facing hemisphere enabled by its geostationary orbit, the LIS on TRMM had the advantage of coincident microphysical measurements of the thunderstorms responsible for its flashes. The TRMM sensor package (Kummerow et al., 1998) included a Visible and Infrared Scanner (VIRS), a Precipitation Radar (PR) and the TRMM Microwave Imager (TMI). As the swaths of these scanning instruments were centered on the satellite track, the region bounded by the instrument with the narrowest swath (the PR at ~215 km) was covered by a uniquely-comprehensive set of overlapping measurements of the extent, intensity, and three-dimensional structure of storms below the satellite.

We previously co-located PR, TMI, and VIRS pixels with LIS pixels to generate a database of “Illuminated Cloud Features” (ICFs: Peterson et al., 2016) describing the local thunderstorm environment where lightning was detected. It should be noted that the reliance on LIS event pixels rather than group centroids in the construction of ICFs means that clouds that are illuminated by lightning but do not participate in the lightning discharge will still contribute to the feature (hence their description as illuminated cloud feathers rather than lightning features). Comparing the maximum and minimum microphysical properties of each feature allows us to differentiate between lightning that occurs entirely within the thunderstorm and lightning that happens to illuminate nearby clouds due to favorable radiative transfer conditions.

We previously used these features to define two classes of optical superbolts: “anvil superbolts” that primarily illuminate non-raining clouds at the edge of the storm, and “stratiform superbolts” whose illumination primarily occurr in regions with raining stratiform PR pixels. Anvil superbolts are expected to benefit from relatively-clear sight lines from the source to the satellite (for example, reflecting of the sides of nearby clouds), potentially making normal lightning appear brighter than it otherwise would. Such “shortcut” paths are not anticipated for stratiform superbolts, which are expected to be bright due to the physical attributes of the discharge, alone.

We will take a closer look at ICFs in this study, placing a particular emphasis on thunderstorms that generate the most energetic LIS pulses in the superbolt hotspots that fall within the TRMM domain.

3 Results

In the following sections, we will examine the various aspects of lightning physics and optical lightning detection that influence whether a lightning pulse will be detected as a superbolt. In Section 3.1, we will address the issue of identifying superbolts by peak optical power or total optical energy and reconcile the PDD estimated broadband source powers / energies reported in Peterson and Kirkland (2020) with the local thresholds on narrowband GLM energy used by Peterson and Lay (2020). In Section 3.2, we will examine the effects of instrument triggering and platform orbit on the types of superbolts that are resolved by the FORTE PDD and GLM. Section 3.3 will, then, use ICFs to analyze the thunderstorm environments responsible for intense optical emission. Finally, Section 3.4 will leverage the staring GLM coverage to document how the physical development of lightning flashes drives optical superbolt outputs.

3.1 Identifying Superbolts in Peak Optical Power and Total Optical Energy Measurements

Superbolts were originally identified according to peak optical power in Turman (1977), who proposed a minimum broadband power threshold of 100 GW estimated at the source. To identify superbolts using integrating instruments like LIS or GLM, we need to identify a total narrowband energy threshold that captures the population of lightning with that exceeds the peak broadband optical power threshold. Because total optical energy is simply a product of the amplitude and shape of the optical waveform, the two parameters are highly correlated and the samples should be at least similar to the first order.

A more accurate picture of the relationship between peak optical power and total optical energy is shown in Figure 1, which depicts the tail of the PDD power and energy distribution. Note that the steps in the plot around 20 MW and 400 MW are not physical, but instead due to the PDD's pricewise-linear response curve. For each optical power, there is a range of possible optical energies that depends on the distribution of lightning pulse shapes. Very impulsive events (like -CGs) are located at the bottom of the distribution where total energies are low for a given power while very broad events (like +CGs) are located at the top of the distribution where energies are high for a given power. The first percentiles (bottom dotted line) and mean energies (solid line) for each power are overlaid as line plots.

Switching from a peak power threshold to a total energy threshold requires shifting our focus from a vertical cut in Figure 1 to a horizontal cut. The same energy can be reached with broad events that have low optical powers (left side of the distribution) or quick events with high optical powers (right side of the distribution). Line plots corresponding to the first percentile (left dotted line) and mean (dashed) powers for each energy are also overlaid in Figure 1. The solid and dashed lines are usually close to one another and nearly overlap above 100 GW. This means that the average energy for a 100 GW PDD event is 44 MJ and the average power for a 44 MJ PDD event is ~100 GW. Thus, a threshold of 44 MJ might be considered an acceptable broadband total energy analog for our 100 GW superbolts.

However, assigning a threshold based on the mean total energy will admit events that are not powerful enough to be considered superbolts into the sample. If we wanted to ensure that 99% of the sample described 100 GW superbolts, we would need to increase the threshold to 120 MJ where the left dotted first percentile curve reaches 100 GW. At this point, the mean optical power for all events that meet this threshold would be 300 GW and most superbolts would be excluded along with the events that did not meet the optical power definition of a superbolt. Alternatively, if we wanted to allow less-powerful events in order to not lose any peak power superbolts from the sample, we would set the threshold to the first percentile of event energy for 100 GW superbolts, which is 20 MJ. Thus, the equivalent total energy threshold for a 100 GW optical power might range from 20 MJ to 120 MJ, depending on the desired composition of the resulting sample.

Figure 2 shows global distributions of PDD events using a 100 GW peak power threshold (Figure 2a) and the 44 MJ total energy threshold (Figure 2b). Figure 2c, then, computes the percentage of 44 MJ events that are not 100 GW superbolts in each mapped bin. The broad trends in the global distributions for each threshold are largely the same. There are hotspots over Panama, the Congo Basin, and the Maritime Continent where normal lightning can be particularly powerful / energetic and regional maxima in the South Pacific Convergence Zone, Mediterranean Sea, western China, and the oceanic regions surrounding Japan. The largest differences in the two maps are found within 30 degrees latitude of the equator, and few 44 MJ events are not also 100 GW superbolts in the mid-latitude superbolt hotspot regions (i.e., the local maxima in Figure 2a plus the oceanic regions south of 30° S). Using mean total energy as an equivalent threshold for peak optical power will add non-superbolt events, but these events do not appear to affect the general superbolt trends.

However, we also have to recognize that the 100 GW superbolt threshold proposed by Turman (1977) is largely arbitrary. It coincides with the tail of the lightning distribution, but Figure 2 shows that the population of PDD events at this peak power is predominantly normal lightning in the usual lightning hotspots that just happen to have high optical powers. Higher thresholds (like 350 GW) are required for the anomalous behavior of superbolts to become apparent in the distribution – and even Turman (1977) placed a greater emphasis on higher threshold of 1 TW in their discussion of superbolts. It is advantageous to examine not just one superbolt total energy threshold, but multiple possible thresholds, and then consider how the population of lightning events changes between them. Even lower thresholds like 20 MJ that are dominated by non-superbolt lightning can be used to reveal the meteorological conditions that lead to energetic lightning, while the lower threshold provides a larger thunderstorm sample for evaluating statistical trends.

Considering multiple energy thresholds is particularly important for LIS and GLM because there is not a one-to-one relationship between broadband optical energy and the narrowband energy at 777.4 nm. The fraction of the signal at the Oxygen emission multiplet is not uniform between flashes, and we cannot infer its spectral content (and thus, equivalent broadband energy) for each individual LIS / GLM pulse. Two values have been derived in the literature for the percent of the broadband energy that is contained at 777.4 nm: ~1% based on ground-based measurements from return strokes (Orville and Hendersen, 1984) and 4% from FORTE PDD observations (Suszcynsky et al., 2001), demonstrating a considerable range in spectral content between optical pulses.

Table 1 lists the LIS / GLM 777.4 nm total energy thresholds that we consider from the tail of the optical energy spectrum. The approximate equivalent broadband energies, ratios between the threshold and normal lightning energies, and the number of LIS / GLM / PDD events that meet the threshold are also listed. The lowest threshold is 0.1 MJ, which would correspond to a broadband energy between 2.5 MJ (4%) and 10 MJ (1%). In either case, this threshold is below the superbolt range discussed previously. It is chosen to ensure a large sample of TRMM ICFs for examining the attributes of thunderstorms that generate energetic lightning.

The second narrowband energy threshold is 0.5 MJ. Assuming a spectral content of 1%, the broadband energy equivalent for this threshold is close to the mean energy for 100 GW superbolts (44 MJ) discussed previously. However, under a 4% spectral energy content, this threshold would only be equivalent to just 12 MJ. The ratios of the thresholds to the mean lightning energy might provide some insight into which spectral content fraction is more reasonable for superbolts. The peak power threshold of 100 GW from Turman (1977) is close to 100x more powerful than normal lightning, and the PDD data support this. For LIS and GLM, a narrowband threshold of 0.5 MJ is 116x (LIS) and 102x (GLM) the energy of normal lightning. Applying the same threshold to the PDD events under a 1% assumption would be equivalent to 33x normal PDD lightning, while a 4% spectral content would correspond to just 8x normal lightning. Due to limitations in instrument design and how the PDD was commanded to trigger over the FORTE mission, we do not expect the amount of in-cloud lightning captured by the PDD to match LIS and GLM. Thus, the average PDD event energy will be different, leading to the different ratios in Table 1. However, of the two spectral contents considered, 1% appears to be more consistent with the top LIS / GLM detections.

Under this 1% assumption, a narrowband threshold of 0.5 MJ yields 11,568 PDD events (on the same order of magnitude as the >100 GW sample in Peterson and Kirkland, 2020) while a 1.0 MJ threshold yields 2,641 PDD events, and a threshold of 2 MJ yields 309 PDD events. These events were collected by the PDD over a 12-year period that lasted from late 1997 until 2010. The LIS instrument on the TRMM satellite, meanwhile, recorded 14,912 optical pulses with narrowband energies > 0.5 MJ (3,109 within the PR swath), 655 (107) pulses > 1.0 MJ, and 9 (0) pulses > 2 MJ over a 15-year period.

The Low Earth Orbit of FORTE and TRMM provided coverage of all longitudes, but at the expense of a limited view time over the thunderstorms in each region. The staring hemispheric coverage of GLM allows it to detect superbolts whenever they occur within its FOV. As a result, just two years of GLM observations have yielded 1,491,010 optical pulses matched with WWLLN strokes that have narrowband energies > 0.5 MJ, 226,814 pulses > 1.0 MJ, 21,869 events > 2.0 MJ, and even 1,288 events > 4.0 MJ. The quantities of high-energy optical pulses detected by GLM eclipse those from any of the other instruments.

3.2 Instrument Effects on Optical Superbolt Detections

While the FORTE PDD, TRMM LIS, and GLM are able to detect superbolts, the design of these instruments and the orbits of their satellite platforms pose challenges for documenting robust global statistics. The instruments in low Earth orbit (PDD, LIS) have difficulty detecting superbolts due to their limited view times. However, the PDD has an additional limitation in its maximum trigger rate. Superbolts that occur early in the flash can be readily detected by the PDD, but intense optical emissions that occur hundreds of milliseconds after the start of the flash (as we see with long-horizontal stratiform flashes) might be missed.

Figure 3 generates statistics on superbolt timing relative to the start of the flash for the PDD (red), LIS (blue), and GLM (cyan) events with equivalent narrowband energies > 0.5 MJ. Histograms are shaded with circle symbols overlaid while Cumulative Distribution Functions (CDFs) are presented as solid lines. Despite the differences in their observational domains, the LIS and GLM distributions are quite similar with an initial peak at the flash start (i.e., the first bin at 1 ms) and then a later delayed peak at ~300 ms into the flash. While we are looking at the top LIS / GLM detections in these statistics, the same behavior occurs with all substantially-energetic optical pulses (i.e., Figure 5 in Peterson and Rudlosky, 2019).

Of these two peaks in the LIS / GLM distributions, the later peak is the more prominent. Most of the LIS / GLM optical pulses that exceed 0.5 MJ occur late in the flash, with only 2-3% occurring in its first milliseconds. The PDD, meanwhile, has difficulty detecting superbolts in this later peak. Both peaks are visible in the PDD data, but 69% of the PDD superbolts occur in the first peak at the beginning of the flash. Thus, the PDD superbolts that we reported previously in Peterson and Kirkland (2020) are only a subset of all superbolts, which might be better described by LIS or GLM, as they are not subject to this maximum trigger rate issue.

However, the GLM optical energy distributions are also subject to significant biases from look angle, which may also exist to a lesser extent for the PDD or LIS. Figure 4 plots distributions of PDD (a), LIS (b), and GLM (c) estimated narrowband source energies as a function of the elevation angle of the satellite over the lightning source. As the PDD lacks geolocation information, we compute look angles for PDD matches to NLDN strokes, leading to overall higher energies at all elevation angles compared to the LIS and GLM total lightning curves. PDD source energies do not vary notably with elevation angle, resulting in flat mean (solid) and median (dashed) curves.

The LIS distribution (Figure 4b) is mostly flat, but there is a slight increase in source energy at lower elevation angles. Much of this deviation comes from the lack of the lowest-energy optical pulses closer to the edge of the LIS FOV. But some of the single most energetic LIS pulses also come from lower elevation angles. This trend reflects the overall distribution of lightning as a function of look angle and is probably unrelated to instrument sensitivity.

We show the GOES-17 GLM distribution in Figure 4c to limit biases from comparing land to ocean lightning. As with LIS, the GLM energy distribution is largely flat at high elevation angles. However, between 40 and 50 degrees, the energy distributions begins to trend upward towards more radiant optical pulses. Part of this shift is the erosion of particularly-faint optical pulses closer to the edge of the GLM FOV, similar to what we saw with LIS. However, we also see a pronounced increase in the energies of the mid-range and particularly radiant GLM detections. As these GLM groups are matched with WWLLN strokes, this increase in energy cannot be explained by the sunrise / sunset solar artifacts we examined previously (Peterson, 2020). Instead, it appears to be caused by the side view of the storm at the edge of the GLM FOV. When GLM can see below the overhanging anvil clouds surrounding the convective core, it has a relatively clear path to the optical source compared with transmitting through the full optical depth of convective cloud.

We previously mitigated these look angle biases by defining local GLM superbolt thresholds based on the energy statistics of the lightning at each location across the GLM domain. As all lightning at a given look angle would be impacted by these effects, not just superbolts, this approach was sufficient to identify exceptional cases out to low elevation angles. To permit the use of a constant energy threshold (as in Turman, 1977 and Peterson and Kirkland, 2020) from GLM's hemispheric geostationary perspective, we will mark problematic elevation angles in geospatial GLM analyses and omit regions with elevation angles lower than 50 degrees in the GLM statistics in the following sections.

Viewing the thunderstorm from the side is not the only scenario where superbolts might arise from a direct line of sight on the lightning channels. Exposed lightning channels that leave the cloud medium could also give rise to favorable viewing conditions. Indeed, some schematic diagrams of superbolts in popular media depict superbolts as cloud-to-air discharges. We can assess the feasibility of this explanation by looking for a key signature of exposed lightning channels in GLM observations: high concentrations of optical energy in individual GLM pixels encompassing the channel. This was a key metric for Gigantic Jet cases (Boggs et al., 2019) (GLM does not detect the jet, but rather the leader leaving the cloud top). The fraction of the

GLM group energy in a single event also helps us to discern between optical sources originating at different altitudes in the cloud (Peterson et al., 2022).

We plot event energy fractions against group energy for superbolt cases with elevation angles > 50 degrees in the two-dimensional histogram in Figure 5. Groups close to the 0.5 MJ threshold range from cases with the energy spread nearly evenly across the group footprint (~0 %) to cases with nearly all of the group energy contained within a single event pixel (~100%). However, as we move towards more energetic superbolts, fewer cases have high concentrations of energy while the group energies generally becomes spread over progressively larger areas. The intense optical outputs from superbolts thus arise from the extensive illuminated lightning channels within the clouds and scattering effects from the cloud medium rather than upward leaders leaving the cloud top.

3.3 Thunderstorm Environments where Energetic Lightning Occurs

We use our ICF database to examine the microphysical properties of the storm regions that are illuminated during the energetic optical pulses detected by LIS on the TRMM satellite. We consider the lower 0.1 MJ narrowband threshold to ensure a robust sample size and include only the optical detections that occur entirely within the narrow PR swath. The global distribution of these energetic LIS detections is shown in Figure 6a, while the most common month of the year and local solar hour are presented in Figure 6b and c. Note that these distributions have not been normalized according to instrument viewtime in order to highlight thr quantities of lightning activity have been detected by TRMM-LIS in the mid-latitude regions from our discussion of Figure 2.

As with Figure 2, the energetic LIS lightning distributions have peaks in the tropical hotspots for normal lightning. However, since LIS provides accurate geolocation information that is unavailable to all PDD events, we can note fine-scale regional variations with LIS that were spread over a large area in the PDD distribution. The energetic lightning distribution is enhanced over coastal Central America and certain mountain ranges - including the Andes highlighted by Holzworth et al. (2019). The top WWLLN events may not rise to the optical intensities of superbolts, but they still might represent energetic lightning. The temporal distributions of superbolts also vary considerably across the TRMM domain. The mid-latitude oceanic superbolt hotspots in the Mediterranean Sea, the southern Pacific Ocean, and the seas surrounding Japan have a wintertime nocturnal-to-morning dominance in Figure 6b,c consistent with Turman (1977). However, the remaining global regions have large variations in peak month / hour that depend on local weather patterns. For example, the south-central United States in North America and the La Plata basin in South America tend to peak in the spring-to-summer months and the La Plata basin has a pronounced overnight maximum in Figure 6c, consistent with the climatology of megaflash activity (Peterson, 2021b). Energetic optical sources elsewhere over land tend to peak during the day and might occur at different points of the year.

The distributions in Figure 6b,c are complex because we are aggregating multiple types of energetic optical pulses that have their own annual / diurnal cycles. The radiant energy of a lightning pulse depends on physical attributes of the flash as well as radiative transfer effects within the surrounding cloud medium, and fewer favorable factors are required to meet such a low threshold (0.1 MJ) than the higher thresholds listed in Table 1. This is demonstrated in

Figure 7, which shows the average PR raining fraction, minimum TMI 85 GHz Polarization Corrected Temperature (PCT), PR maximum storm height, and VIRS gradient in infrared brightness temperature for the ICFs in each region. The mid-latitude superbolt hotspots from the prior PDD analyses correspond to markedly different thunderstorm environments than the energetic optical pulses across the tropics. The storm regions illuminated by the mid-latitude energetic pulses are almost entirely bounded by PR rainfall, have limited column-integrated ice mass based on the minimum 85 GHz PCT signature, have low storm heights for electrified storms, and have small differences in VIRS infrared brightness temperature across the feature.

The energetic optical pulses in the superbolt hotspot regions occur in stormclouds that are shallow and homogeneous, apparently lacking intense updrafts – consistent with our previous discussion of stratiform superbolts. Meanwhile, energetic LIS detections from across the tropics (particularly over land) illuminate significant fractions of non-raining clouds with lower 85 GHz PCTs that are also taller with large gradients in infrared brightness temperature – all indicating intense convection, as one would expect with anvil superbolts where light can escape the side of a convective thunderstorm region to illuminate nearby clouds.

We previously reported that anvil superbolts are the more common scenario, with up to 2% of all flashes producing an anvil superbolt (Peterson et al., 2020). However, the prevalence of superbolts illuminating primarily the non-raining clouds surrounding the convective core varies globally (as shown in Figure 7) and according to the selected energy threshold. Figures 8 and 9 elaborate on the cloud types illuminated by superbolts by generating similar cloud-type fraction plots to Figure 2 in Peterson et al. (2020) from the 0.1 MJ (left panels) and 0.5 MJ (right panels) LIS optical pulses. Two distinct regions of the TRMM domain are shown for comparison: the inner tropics (10° S – 10° N), and the northern mid-latitude regions (30° N – 36° N).

LIS detections in the inner tropics are presented in Figure 8. The top panels (Figure 8a,b) show two-dimensional histograms of event count as a function of the raining stratiform areal fraction and raining convective areal fraction of the ICF, each weighted by event count. The three vertices of the triangles in these plots represent entirely convective flashes (top left), entirely stratiform flashes (bottom right), and entirely anvil flashes (bottom left). Solid lines are drawn to distinguish flashes that have a primary cloud type (> 50% convective, stratiform, or anvil) and the total percent of the sample that has each primary type is listed. Dashed lines, meanwhile, are drawn at the 75% level with the fractions of the sample with > 75% of any type also listed.

ICFs with optical energies > 0.1 MJ in the inner tropics are most frequently either primarily anvil flashes (39%) or a combination of anvil and convective flashes, resulting in a distribution that is concentrated along the left side of the triangle. Only 11% of 0.1 MJ pulses in the inner tropics occur in primarily stratiform flashes. If we increase the threshold from 0.1 MJ to 0.5 MJ, the primarily-stratiform fraction doubles to 23%, mostly at the expense of primarily-convective flashes that fall to 12% of the total, while the anvil fraction remains nearly constant.

The bottom two rows of Figure 8 replace the ICF convective fraction with the maximum PR storm height (Figure 8c,d) or the time of the energetic group in the flash (Figure 8e,f). The maximum PR storm heights for primarily (> 50%) non-stratiform flashes range from < 5 km to 20 km, with a distinct maximum around 15 km. Primarily stratiform flashes, meanwhile, have lower maximum PR storm heights that are typically around 10 km altitude. Increasing the threshold to 0.5 MJ affects the relative frequencies of stratiform / non-stratiform cases and removes most of the non-stratiform pulses that only illuminate clouds with storm heights < 10 km.

The timing of these energetic events within the flash also depends on cloud type. Boundaries and percentages are overlaid in Figure 8e,f between primarily stratiform / non-stratiform cases, and also between cases that occur before or after 12 ms into the flash (corresponding to the minimum in the bimodal distribution). Dashed lines are also drawn to indicate a greater delay of 200 ms, which approximates the point in the flash where the PDD typically reaches its maximum trigger count. While a significant fraction of energetic lightning events in the inner tropics occur early in the flash (30% < 12 ms) - mostly from non-stratiform cases (28%) - the remaining 70% of > 0.1 MJ pulses are delayed. 39% occur > 200 ms into the parent flash where the FORTE PDD would have difficulty detecting them, contributing to its suppressed second peak in Figure 3. The 0.5 M distribution is largely similar aside from the greater proportion of stratiform lightning noted previously.

Constructing the same plot for 0.1 MJ and 0.5 MJ pulses in the northern hemisphere mid-latitudes reveals notably different trends compared to the inner tropics. The cloud type histograms in Figure 9 (a,b) are heavily weighted towards raining events along the right diagonal edge of the cloud type fraction distribution. Only 17% of 0.1 MJ pulses and 12% of 0.5 MJ pulses are primarily anvil cases, with 26% (44%) being primarily stratiform and 41% (23%) primarily convective. The maximum PR storm heights from these cases in Figure 9c,d are also considerably lower than in the tropics – with most energetic stratiform pulses occurring in clouds with storm heights between 5 km and 10 km. At the same time, the fraction of early pulses in the flash is reduced to 13% at 0.1 MJ and 9% at 0.5 MJ.

Other global regions either resemble the inner tropics or northern mid-latitudes, or some combination of the two if they have similar quantities of stratiform / non-stratiform cases. Unfortunately, we do not have enough LIS cases within the PR domain to increase the threshold further. However, the greater prevalence of primarily-stratiform cases with increasing energy threshold suggests that the vertically-compact, low flash rate environments generated by stratiform-like clouds are favorable for the particularly-bright optical pulses at higher thresholds. Expected mechanisms for this are: (1) low flash rates permit more charge storage between flashes, (2) proximity of charge layers to ground facilitating CG strokes (particularly LUTs), and (3) expansive layered charge structures promoting horizontal development, creating a larger optical source while granting the flash access a larger charge reservoir.

3.4 The Top GLM Superbolts and the Relationship between Lateral Flash Structure and Superbolt Energy

Examining the most energetic optical lightning pulses on Earth requires large viewtimes over regions that are known for exceptional lightning. While GLM does not capture the ocean regions surrounding Japan, its FOV does cover the northern and southern Pacific Ocean regions where superbolts are known to occur, as well as the megaflash hotspots from Peterson (2021b).

The top WWLLN-matched GLM cases are plotted in Figure 10 with a 0.1 MJ threshold (Figure 10a), and the distribution largely mirrors the 0.1 MJ LIS distribution from Figure 6a. We increase the threshold to 1.0 MJ in Figure 10b, and this eliminates many of the oceanic cases, as well as cases in the Amazon rainforest. We also start to see enhancements near the edge of the

GLM field of view from look angle biases. Elevation angles of GLM relative to the source are overlaid as dashed contours between 20 degrees and 50 degrees. Increasing the threshold to 2.0 MJ erodes the local maximum along the Andes (including Colombia) and through Central America, while amplifying the low elevation angle biases at the edge of the GLM FOV. Finally, by 4.0 MJ, the primary clusters of GLM superbolts within the 50 degree elevation angle contour correspond to the megaflash hotspots in the Great Plains of North America and the La Plata basin of South America, with sparse detections occurring in some ocean regions (i.e., the north Atlantic Ocean) and in the Amazon region.

The detections at lower elevation angles are still valid cases of energetic lightning. We are just unsure of how energetic they would be if they were observed from a less-advantageous angle. Therefore, we can still use data from the full GLM FOV to generate statistics that describe the relationships between intense optical detections in each region (even if they would not reach the superbolt scale) and their parent flashes, as we did previously with the top LIS cases.

Figure 11 shows the average time in the parent flash for the cases that meet each energy threshold in Figure 10. Figure 3 showed that GLM superbolts are most commonly delayed from the flash start by up to hundreds of milliseconds. However, this is only due to the prevalence of superbolts over land and the tropical oceans where the delays are particularly long in Figure 10. By contrast, the average superbolt occurs within tens of milliseconds from the flash start over the northern and southern Pacific Ocean. Moreover, the most energetic GLM events found in the megaflash hotspots occur even later in the flash. The average delays for the highest thresholds in Figure 11c-d even approach 1 second.

The FORTE PDD distribution is heavily weighted towards the north and south Pacific Ocean because the superbolts that occur in these regions consistently arise before the instrument reaches its maximum trigger rate. There is no similarly-pronounced hotspot over the Great Plains or the La Plata basin simply because these superbolts happen so late in the flash that the PDD would rarely be able to detect them – even if FORTE were in the correct position and time to observe one. Because GLM does not have this trigger rate limitation, the distributions in Figure 10 should be closer to the distribution of the Earth's top superbolts, at least within the 50 degree elevation angle contour.

The superbolts in this central region also highlight factors that are important controls on optical pulse energy. We have already seen that stratiform-like clouds are conducive for generating energetic pulses, and proposed three mechanisms for why that might be. We can test the third mechanism – the lateral extent of the flash – using GLM data. Figure 12 shows two-dimensional histograms of the superbolt time delay from the start of the flash and the flash extent at that time for the thresholds used in Figures 10 and 11. Solid lines are also drawn at 12 ms (as in Figures 8 and 9), and the megaflash threshold of 100 km. For energetic pulses > 0.1 MJ, 8% occur at the beginning of the flash before the flash has had a chance to develop notable lateral structure, 90% are delayed but not megaflashes by this point in time, and 2% are delayed megaflashes. Increasing the threshold to 1.0 MJ events (Figure 12b) removes almost all of the early superbolts while increasing the megaflash fraction to 5%. Continuing to increase the threshold beyond 1.0 MJ further increases the megaflash fraction to 15% by 2.0 MJ and 28% by 4.0 MJ.

Thus, the optical energy of these radiant pulses depends on the lateral growth of the flash as it expands through the surrounding charge reservoir. Early superbolts – like those detected by the PDD – are at a disadvantage for being particularly-energetic because lateral development usually takes time, while oceanic superbolts may be at a general disadvantage because their maximum sizes are smaller than their land-based counterparts (Peterson and Stano). However, these disadvantages are offset by one primary advantage in these oceanic cases: faster horizontal development speeds that allow the parent flash to grow into a long horizontal flash (or even a megaflash) in the tens of milliseconds before the superbolt. Figure 13 shows the horizontal development speeds measured by GLM for oceanic superbolt-producing flashes. While the coarse pixels and long integration frames of GLM inhibit accurate measurements of the speeds of faster leaders, there is still a notable difference between the land-based and tropical ocean flashes that propagate horizontally around $1x10^5$ ms^{-1} and the mid-latitude oceanic that are multiple times faster - even approaching $1x10^6$ ms^{-1} in some cases. Our analyses of these individual cases, which are not shown for brevity, indicate that the fast bidirectional development modes described in van der Velde et al. (2014) are relatively common in these regions, leading to the increased GLM flash development speeds in Figure 13.

4 Discussion and Conclusion

This study examines the most exceptional optical lightning pulses detected by the FORTE PDD, TRMM LIS, and GLM in order to improve our understanding of how they arise and reconcile differences in the geographic distributions of superbolts detected by each sensor.

We were able to confirm that the PDD maximum trigger rate is limiting the sample of superbolts that it was able to detect. Both LIS and GLM are able to detect energetic events that occur hundreds of milliseconds to multiple seconds into their parent flash that are missed by the PDD. However, LIS and GLM have limitations of their own that need to be considered. GLM, in particular, is biased by favorable look angles near the edge of its FOV. Optical emissions are typically blocked by the anvil clouds that surround the convective core of a thunderstorm. When instruments like GLM observe the storm from the side, these emissions are able to transmit to the sensor along relatively cloud-free paths, increasing the apparent energies of otherwise normal optical pulses. LIS, meanwhile, is primarily limited by the low view times permitted by its orbit. It is unlikely that the TRMM satellite would be located at the right place and time to observe the Earth's most intense superbolts.

Despite these differences, the top PDD, LIS, and GLM detections still represent the brightest optical lightning emissions on Earth. For this reason, we can expect that these top detections arise in similar thunderstorm environments that are favorable for particularly-energetic discharges. Coincident TRMM measurements confirm that "anvil superbolts" are most common at low energy thresholds. These energetic optical pulses illuminate mostly non-raining clouds around the edge of the convective core of the thunderstorm where favorable paths exist for transmitting optical signals to space. This can allow even normal lightning to be identified as a superbolt. However, increasing the suoperbolt threshold increases the proportion of "stratiform" superbolts that occur entirely within raining regions of homogeneous clouds that would not be conducive to such "shortcut" paths to the satellite. The low flash rates, widespread rainfall, limited storm heights, and small gradients in infrared brightness temperature associated with stratiform superbolts are common over the oceanic regions around Japan and in the Mediterranean Sea identified as superbolt hotspots by Turman (1977.

The vertically-compact, stratiform nature of these clouds, as well as in the land-based megaflash cases that we identified in Peterson and Lay (2020), is expected to allow them to store more charge between flashes, which is then mobilized in spectacular fashion during the superbolt. The proximity of the charge layers to ground appears to facilitate CG strokes along the paths taken by these horizontal discharges through the cloud that are able to draw current from the expansive network of lightning channels. Thus, the most energetic superbolts detected by GLM – those that are associated with megaflashes and are on the order of 1000x brighter than normal lightning – occur exclusively late in the discharge after the flash has had ample opportunity to develop laterally to form complex networks of extensive lightning channels.

Acknowledgments

Los Alamos National Laboratory is operated by Triad National Security, LLC, under contract number 89233218CNA000001. The FORTE PDD and GLM superbolt data used in this study are available at the Harvard Dataverse via DOI: 10.7910/DVN/RV39JT, (Peterson, 2020c). Reprocessed GLM data are available from the NASA Global Hydrometeorology Resource Center DAAC at DOI: 10.5067/GLM/CIERRA/DATA101 (Peterson, 2021c).

References

Blakeslee, R. J., Lang, T. J., Koshak, W. J., Buechler, D., Gatlin, P., Mach, D. M., ... & Christian, H. (2020). Three years of the lightning imaging sensor onboard the international space station: Expanded global coverage and enhanced applications. *Journal of Geophysical Research: Atmospheres*, *125*(16), e2020JD032918.

Boggs, L. D., Liu, N., Peterson, M., Lazarus, S., Splitt, M., Lucena, F., ... & Rassoul, H. K. (2019). First observations of gigantic jets from geostationary orbit. *Geophysical Research Letters*, *46*(7), 3999-4006.

Christian, H. J., R. J. Blakeslee, S. J. Goodman, and D. M. Mach (Eds.), 2000: Algorithm Theoretical Basis Document (ATBD) for the Lightning Imaging Sensor (LIS), NASA/Marshall Space Flight Center, Alabama. (Available as http://eospso.gsfc.nasa.gov/atbd/listables.html, posted 1 Feb. 2000)

Cummins, K. L., & Murphy, M. J. (2009). An overview of lightning locating systems: History, techniques, and data uses, with an in-depth look at the US NLDN. *IEEE transactions on electromagnetic compatibility*, *51*(3), 499-518.

Goodman, S. J., Blakeslee, R. J., Koshak, W. J., Mach, D., Bailey, J., Buechler, D., ... & Stano, G. (2013). The GOES-R geostationary lightning mapper (GLM). *Atmospheric research*, *125*, 34-49.

Holzworth, R. H., McCarthy, M. P., Brundell, J. B., Jacobson, A. R., & Rodger, C. J. (2019). Global distribution of superbolts. *Journal of Geophysical Research: Atmospheres*, *124*(17-18), 9996-10005.

Hutchins, M. L., Holzworth, R. H., Rodger, C. J., Heckman, S., & Brundell, J. B. (2012, April). WWLLN absolute detection efficiencies and the global lightning source function. In *EGU General Assembly Conference Abstracts* (p. 12917).

Jacobson, A. R., Holzworth, R., Harlin, J., Dowden, R., & Lay, E. (2006). Performance assessment of the world wide lightning location network (WWLLN), using the Los

Alamos sferic array (LASA) as ground truth. *Journal of Atmospheric and Oceanic Technology*, *23*(8), 1082-1092.

Kirkland, M. W. (1999). An examination of superbolt-class lightning events observed by the FORTE satellite. *Los Alamos National Laboratory, Atmospheric Sciences Group, New Mexico*.

Kirkland, M. W., Suszcynsky, D. M., Guillen, J. L. L., & Green, J. L. (2001). Optical observations of terrestrial lightning by the FORTE satellite photodiode detector. *Journal of Geophysical Research: Atmospheres*, *106*(D24), 33499-33509.

Kummerow, C., Barnes, W., Kozu, T., Shiue, J., & Simpson, J. (1998). The tropical rainfall measuring mission (TRMM) sensor package. *Journal of atmospheric and oceanic technology*, *15*(3), 809-817.

Light, T. E. L., & Jacobson, A. R. (2002). Characteristics of impulsive VHF lightning signals observed by the FORTE satellite. *Journal of Geophysical Research: Atmospheres, 107*(D24), ACL-8.

Mach, D. M., Christian, H. J., Blakeslee, R. J., Boccippio, D. J., Goodman, S. J., & Boeck, W. L. (2007). Performance assessment of the optical transient detector and lightning imaging sensor. *Journal of Geophysical Research: Atmospheres*, *112*(D9).

Peterson, M. (2019a). Using lightning flashes to image thunderclouds. *Journal of Geophysical Research: Atmospheres*, *124*(17-18), 10175-10185.

Peterson, M. (2019b). Research applications for the Geostationary Lightning Mapper operational lightning flash data product. *Journal of Geophysical Research: Atmospheres*, *124*(17-18), 10205-10231.

Peterson, M. (2020a). Modeling the transmission of optical lightning signals through complex 3-D cloud scenes. *Journal of Geophysical Research: Atmospheres*, *125*(23), e2020JD033231.

Peterson, M. (2020b). Removing solar artifacts from Geostationary Lightning Mapper data to document lightning extremes. *Journal of applied remote sensing*, *14*(3), 032402.

Peterson, M. (2020c). Lightning Superbolt Data, https://doi.org/10.7910/DVN/RV39JT, Harvard Dataverse, V2.

Peterson, M. (2021a). Holes in optical lightning flashes: Identifying poorly transmissive clouds in lightning imager data. Earth and Space Science, 8(2), e2020EA001294.

Peterson, M. (2021b). Where are the most extraordinary lightning megaflashes in the Americas?. *Bulletin of the American Meteorological Society*, *102*(3), E660-E671.

Peterson, M. (2021c). GLM-CIERRA. https://doi.org/10.5067/GLM/CIERRA/DATA101

Peterson, M., & Rudlosky, S. (2019). The time evolution of optical lightning flashes. *Journal of Geophysical Research: Atmospheres*, *124*(1), 333-349.

Peterson, M., & Kirkland, M. W. (2020). Revisiting the Detection of Optical Lightning Superbolts. *Journal of Geophysical Research: Atmospheres*, *125*(23), e2020JD033377.

Peterson, M., & Lay, E. (2020). GLM Observations of the Brightest Lightning in the Americas. *Journal of Geophysical Research: Atmospheres*, *125*(23), e2020JD033378.

Peterson, M., Rudlosky, S., & Deierling, W. (2018). Mapping the lateral development of lightning flashes from orbit. *Journal of Geophysical Research: Atmospheres*, *123*(17), 9674-9687.

Peterson, M. J., Lang, T. J., Bruning, E. C., Albrecht, R., Blakeslee, R. J., Lyons, W. A., ... & Cerveny, R. S. (2020). New World Meteorological Organization certified megaflash lightning extremes for flash distance (709 km) and duration (16.73 s) recorded from space. *Geophysical Research Letters*, *47*(16), e2020GL088888.

Peterson, M., Light, T. E., & Shao, X. M. (2021a). Combined Optical and Radio-Frequency Perspectives on a Hybrid Cloud-to-Ground Lightning Flash Observed by the FORTE Satellite. *Journal of Geophysical Research: Atmospheres*, *126*(7), e2020JD034152.

Peterson, M., Light, T. E. L., & Shao, X.-M. (2021b). Combined optical and radio-frequency measurements of a lightning megaflash by the FORTE satellite. *Journal of Geophysical Research: Atmospheres,* 126, e2020JD034411. https://doi.org/10.1029/2020JD034411

Peterson, M. J., Light, T. E. L., & Mach, D. M. (2022). The illumination of thunderclouds by lightning: Part 3: Retrieving optical source altitude. *Authorea Preprints*.

Rudlosky, S. D., Goodman, S. J., Virts, K. S., & Bruning, E. C. (2019). Initial geostationary lightning mapper observations. *Geophysical Research Letters*, *46*(2), 1097-1104.

Suszcynsky, D. M., Kirkland, M. W., Jacobson, A. R., Franz, R. C., Knox, S. O., Guillen, J. L. L., & Green, J. L. (2000). FORTE observations of simultaneous VHF and optical emissions from lightning: Basic phenomenology. *Journal of Geophysical Research: Atmospheres*, *105*(D2), 2191-2201.

Suszcynsky, D. M., Light, T. E., Davis, S., Green, J. L., Guillen, J. L. L., & Myre, W. (2001). Coordinated observations of optical lightning from space using the FORTE photodiode detector and CCD imager. *Journal of Geophysical Research: Atmospheres*, *106*(D16), 17897-17906.

Turman, B. N. (1977), Detection of lightning superbolts, *J. Geophys. Res.*, 82(18), 2566– 2568, doi:10.1029/JC082i018p02566.

van der Velde, O. A., Montanyà, J., Soula, S., Pineda, N., & Mlynarczyk, J. (2014). Bidirectional leader development in sprite-producing positive cloud-to-ground flashes: Origins and characteristics of positive and negative leaders. *Journal of Geophysical Research: Atmospheres*, *119*(22), 12-755.

Table 1. 777.4 nm narrowband energy thresholds, equivalent broadband PDD energies under a 1% and 4% assumption, and the corresponding PDD, TRMM-LIS and GLM counts and mean ratios for each threshold. Note that the 4 MJ threshold is only used for GLM cases.

777.4 nm Narrowband Energy	1% PDD energy at 777.4 nm			4% PDD energy at 777.4 nm			TRMM LIS			GLM*	
								Group Count			
	PDD Energy	Mean Ratio	Event Count	PDD Energy	Mean Ratio	Event Count	Mean ratio	Full FOV	PR swath	Mean Ratio	Group Count
0.1 MJ	10 MJ	7x	116779	2.5 MJ	2x	434160	23x	398897	120612	20x	19715511
0.2 MJ	20 MJ	13x	49075	5 MJ	3x	225708	47x	143929	39450	41x	7534022
0.5 MJ	50 MJ	33x	11568	12.5 MJ	8x	90623	116x	14912	3109	102x	1491010
1 MJ	100 MJ	66x	2641	25 MJ	17x	36393	233x	655	107	204x	226814
2 MJ	200 MJ	132x	309	50 MJ	33x	11568	466x	9	0	408x	21869
4 MJ										816x	1288

* Matches with WWLLN strokes required to remove solar artifacts

LA-UR-23-24435

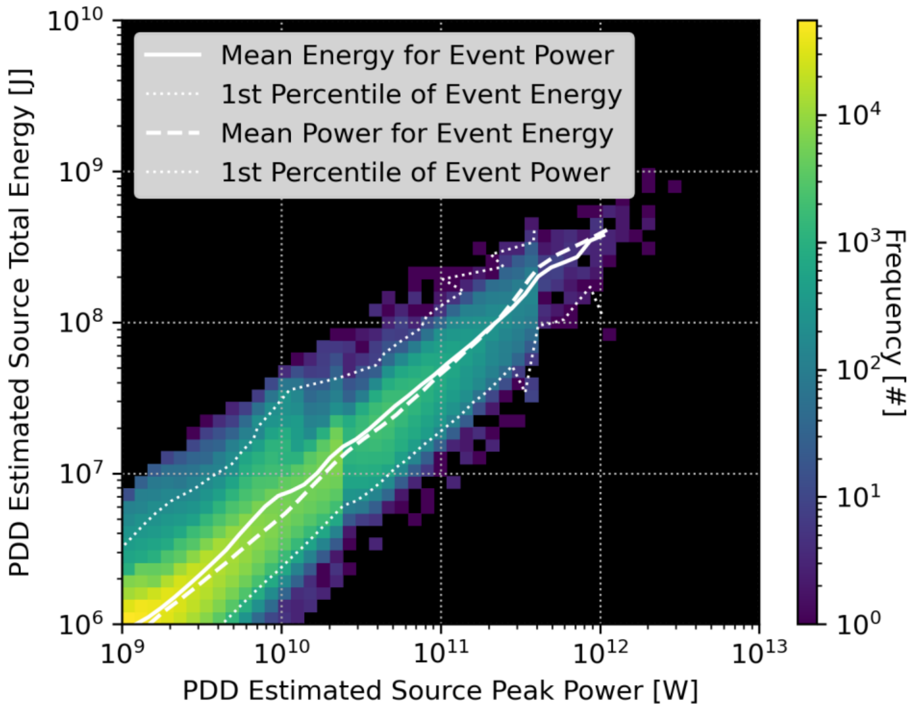

Figure 1. Two-dimensional histogram of peak optical power and total energy of the top PDD events normalized to the source altitude. Solid (lower dashed) lines show the median (1st percentile) energy for each peak power. Dashed (left dotted) lines show the mean (1st percentile) of peak power for each total energy.

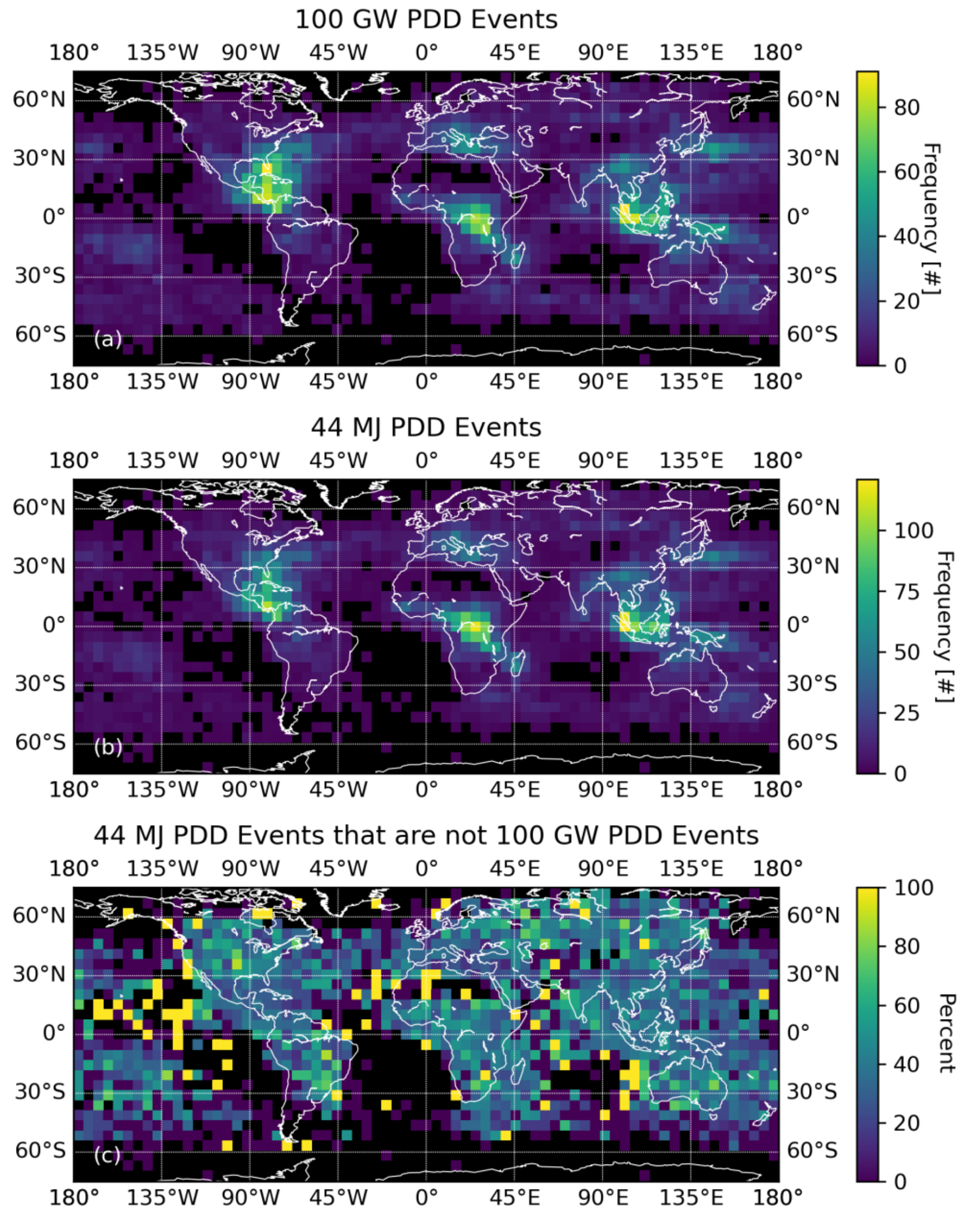

Figure 2. Global distributions of (a) 100 GW peak optical powers and (b) 44 MJ total energies at the source, and (c) fractions of 44 MJ events that are not 100 GW superbolts.

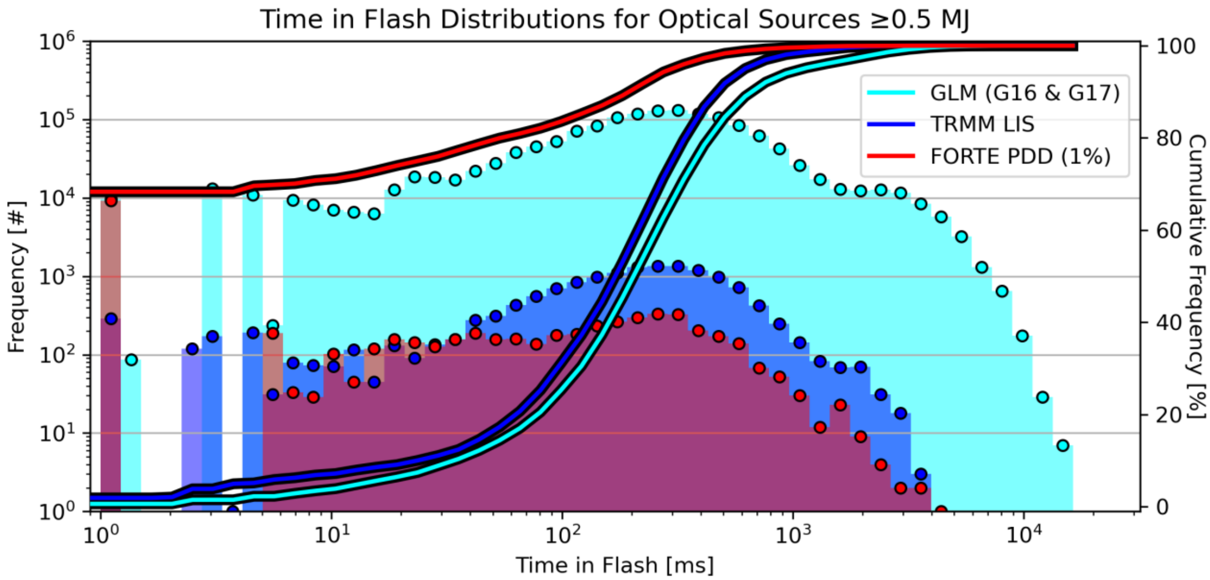

Figure 3. Histograms (dots) and Cumulative Density Functions (lines) of the time in the parent flash when FORTE PDD (red), TRMM LIS (blue), and GLM (cyan) pulses (PDD events LIS/GLM groups) with an equivalent narrowband optical energy at 777.4 nm ≥0.5 MJ occur. For the PDD, it is assumed that the narrowband energy is 1% of the broadband energy.

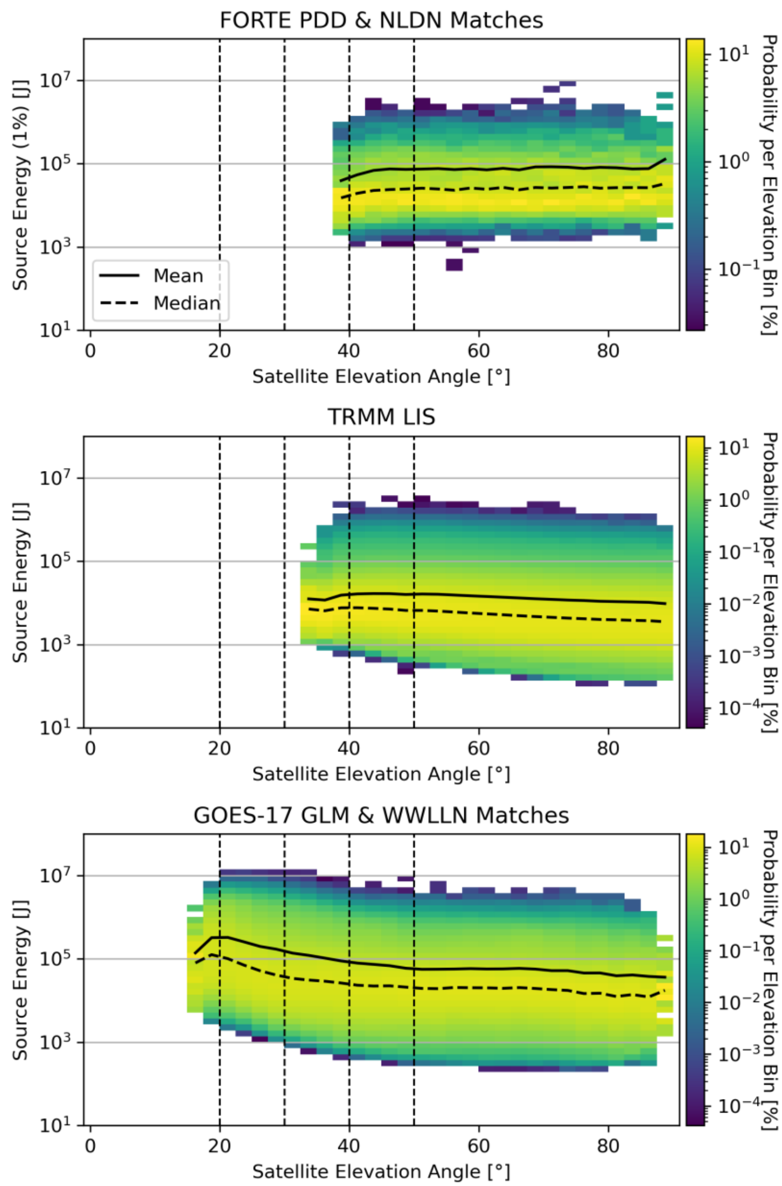

Figure 4. Histograms of narrowband optical energy normalized to the source by satellite elevation angle for (a) FORTE PDD events matched to NLDN, (b) TRMM LIS groups, and (c) the GOES-17 GLM groups matched with WWLLN strokes. Each column sums to 100%, while solid (dashed) lines indicate the mean (median) values. Elevation angles of 20°, 30°, 40°, and 50° are indicated with vertical dashed lines.

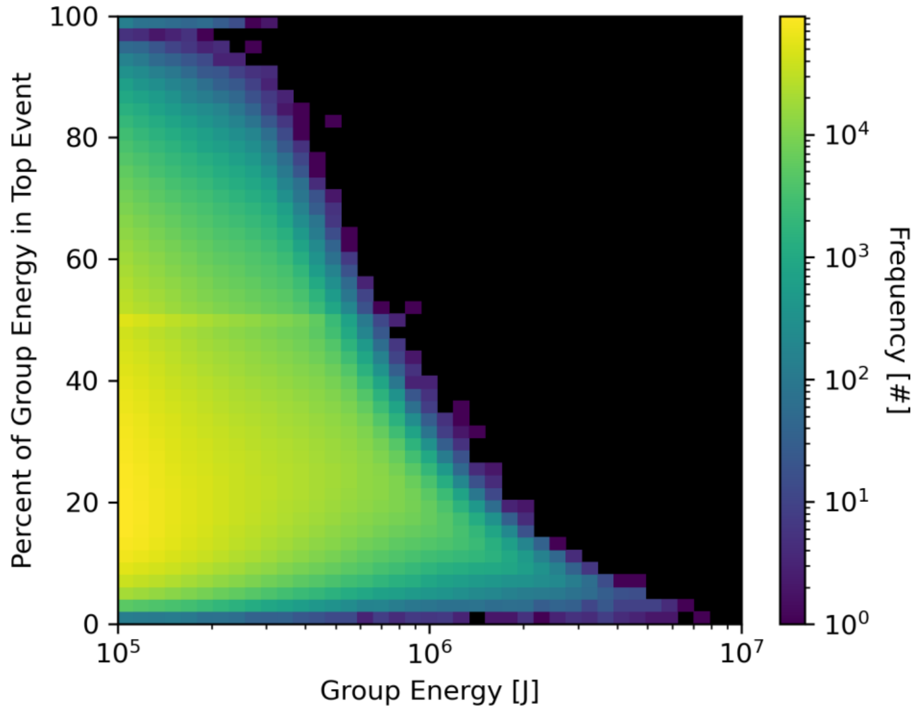

Figure 5. Two-dimensional histogram of GLM group energy and the percent of the overall group energy contributed by the single brightest event pixel for particularly-energetic GLM groups (> 0.5 MJ) from regions of the GLM FOV with elevation angles >50 degrees.

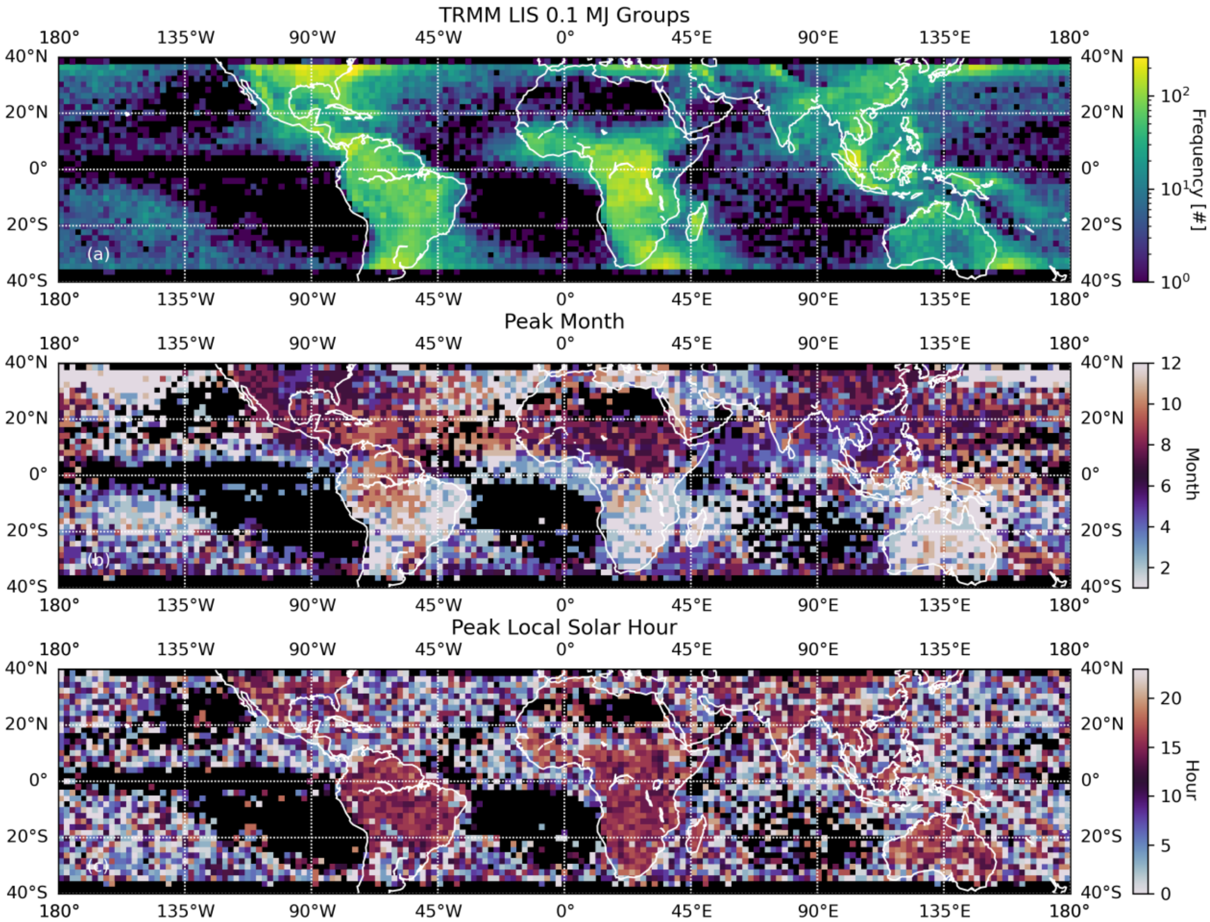

Figure 6. Global distributions of (a) the frequency of TRMM LIS groups with a source energy exceeding 0.1 MJ, and (b) the peak month and (c) the peak local solar hour in which they occur.

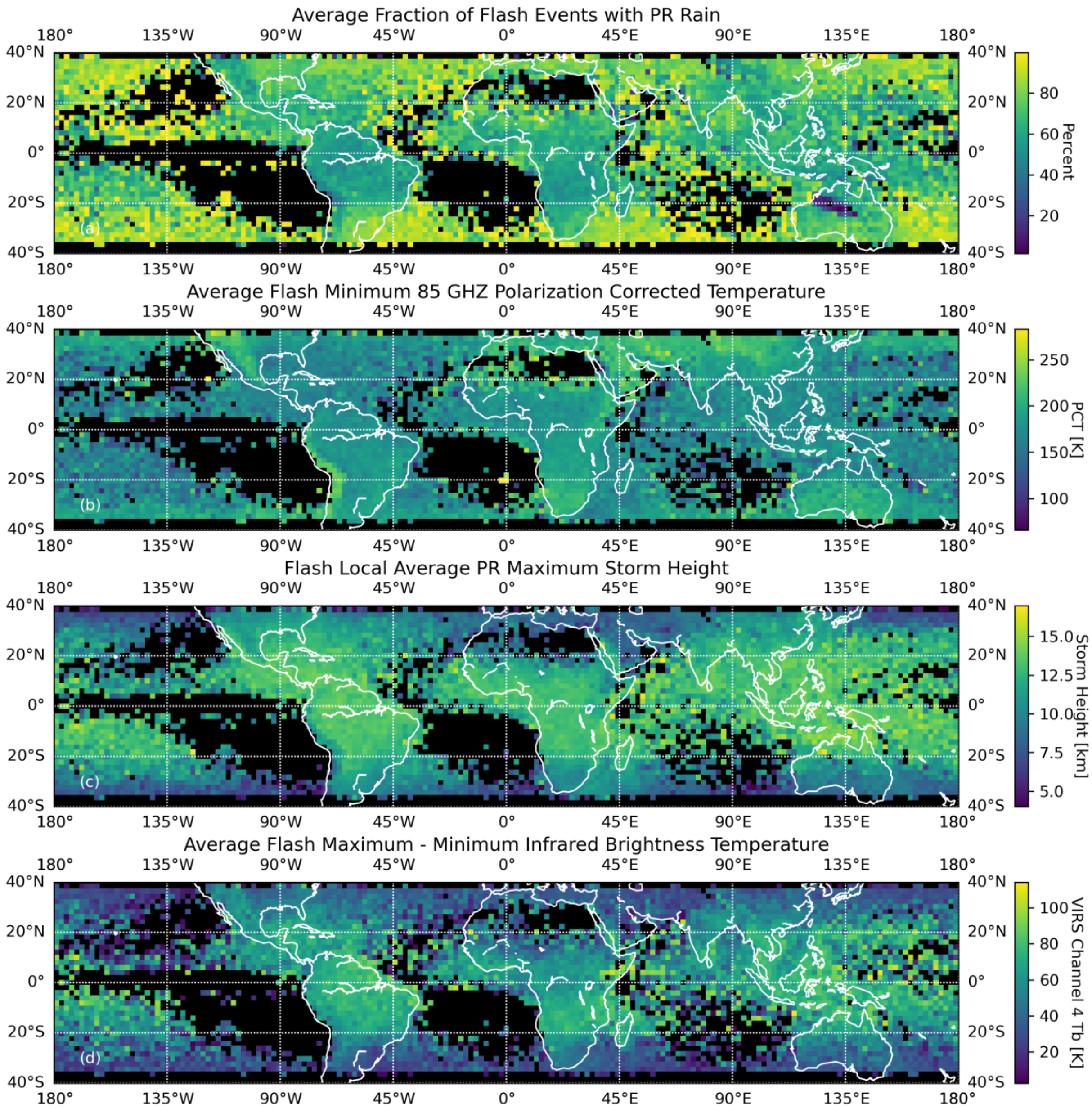

Figure 7. Average characteristics of ICFs that contain >0.1 MJ groups. (a) Average fraction of flashes within PR-detected rainfall. (b) Average minimum 85 GHz PCT. (c) Average PR maximum storm height within the ICF. (d) Average difference in VIRS infrared brightness temperature across the ICF.

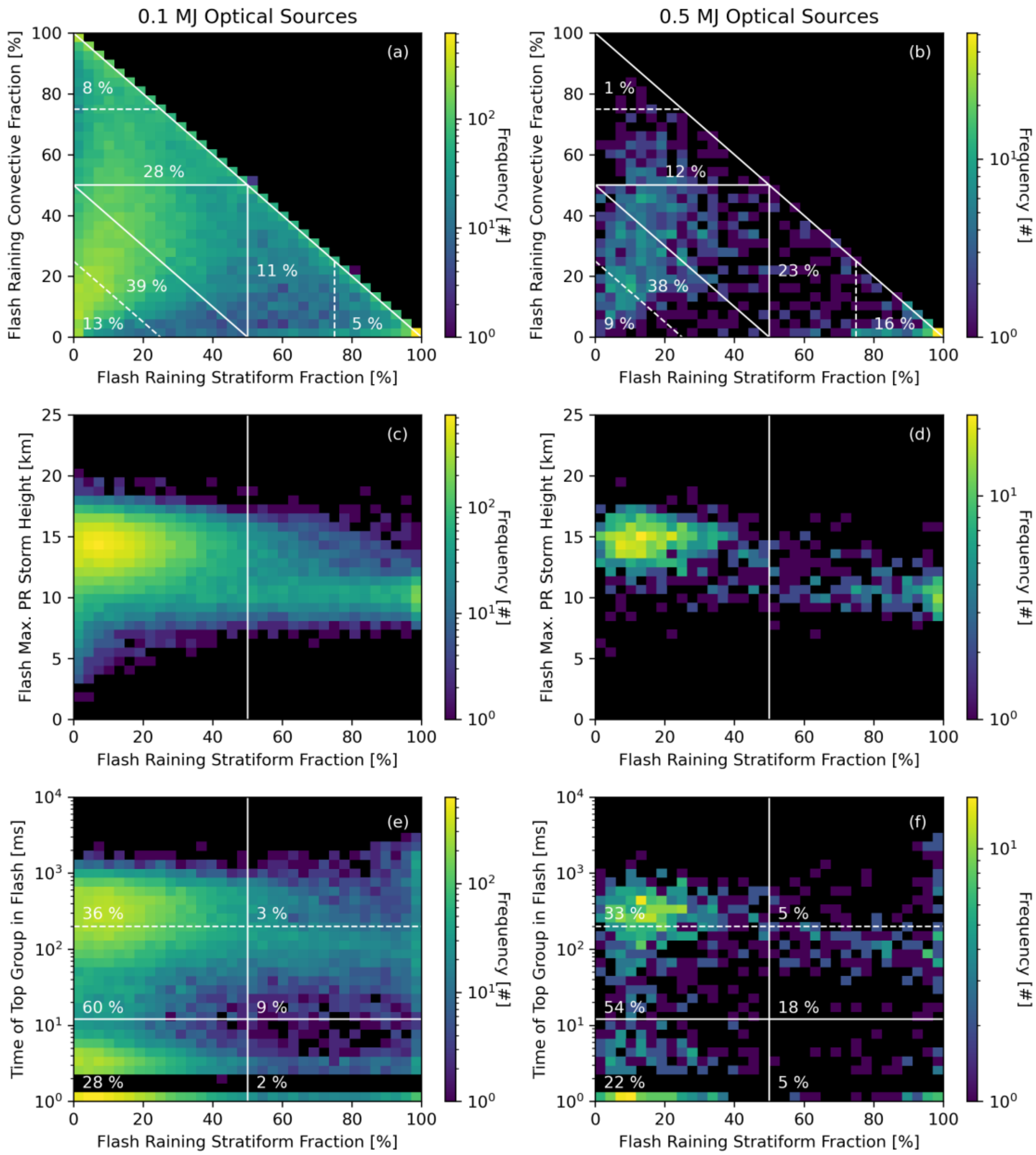

Figure 8. Two-dimensional histograms of ICF raining stratiform area fraction and (a,b) the raining convective area fraction, (c,d) the maximum PR-derived storm height, and (e,f) the time of the most energetic group in the LIS flash in the inner tropics (10° S – 10° N). The left column only includes flashes with groups exceeding 0.1 MJ of optical energy at the source, while the right column requires 0.5 MJ of optical energy. Solid lines indicate flashes that are primarily (>50%) stratiform (all panels), primarily convective or primarily anvil clouds (top panels), or that contain delayed energetic pulses (bottom panels only). Dashed lines indicate flashes with a dominant (>75%) cloud type (top panels) or whose energetic pulse occur at times after the PDD usually stopped triggering (bottom panels).

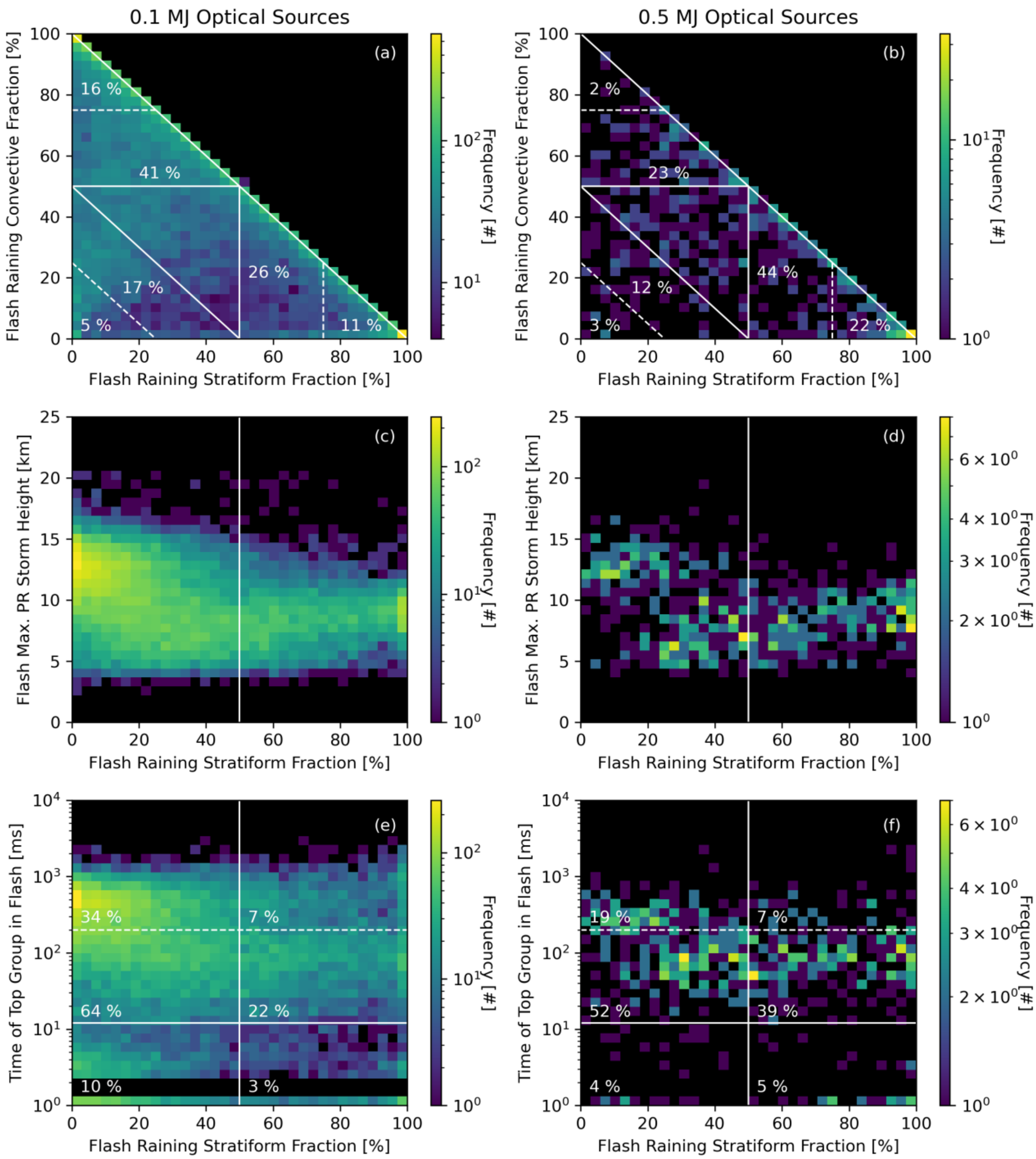

Figure 9. As in Figure 8, but for the northern mid-latitudes (30° N – 36° N).

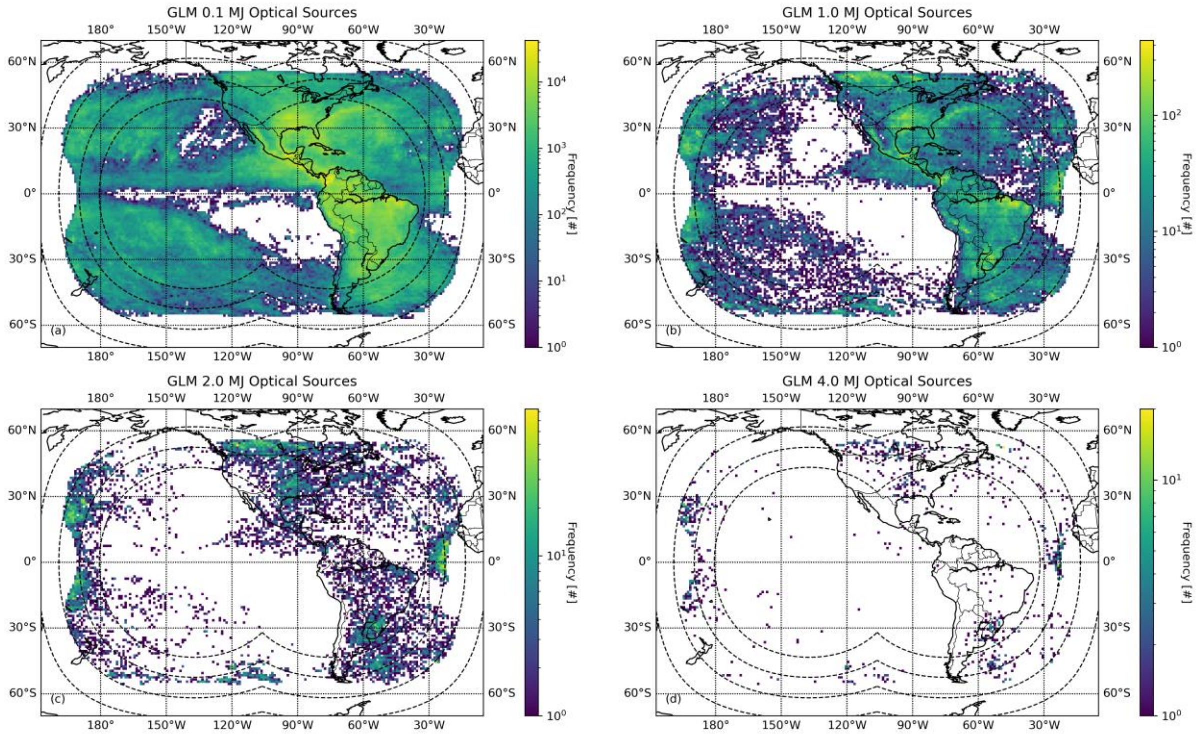

Figure 10. Geographic distributions of GLM optical sources with energies exceeding (a) 0.1 MJ, (b) 1.0 MJ, (c) 2.0 MJ, and (d) 4.0 MJ.

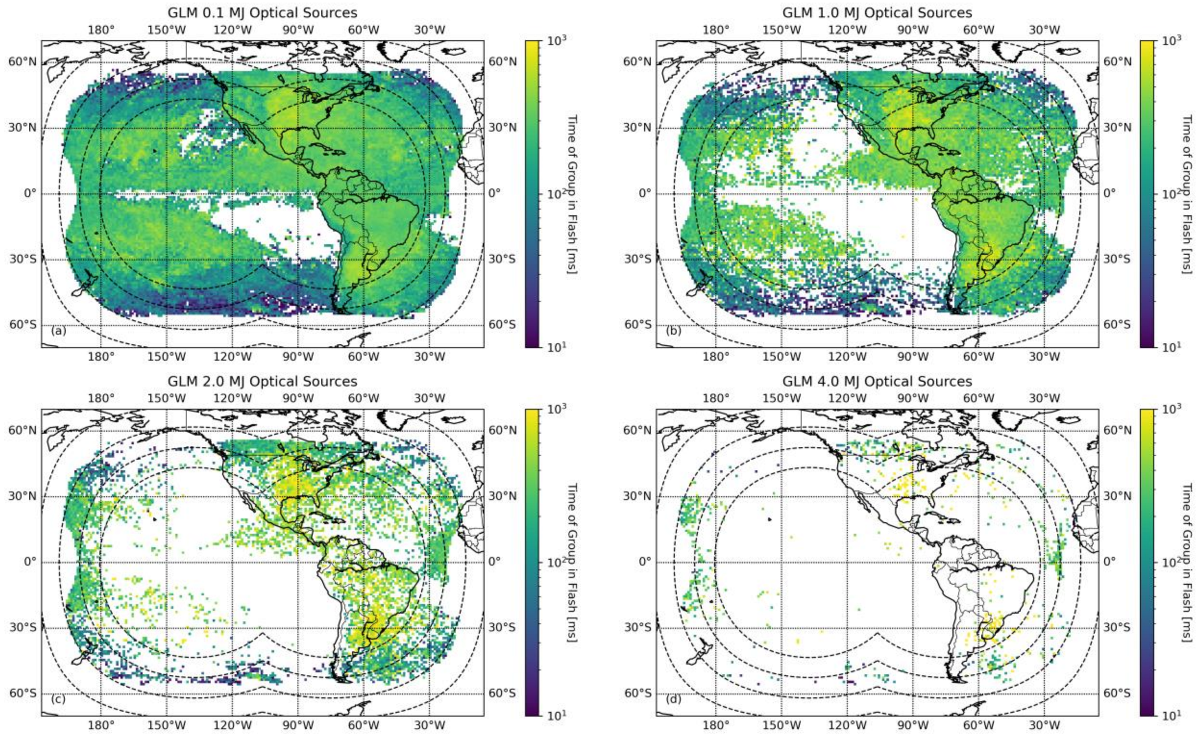

Figure 11. The average time of the energetic groups from Figure 10 in their parent GLM flash.

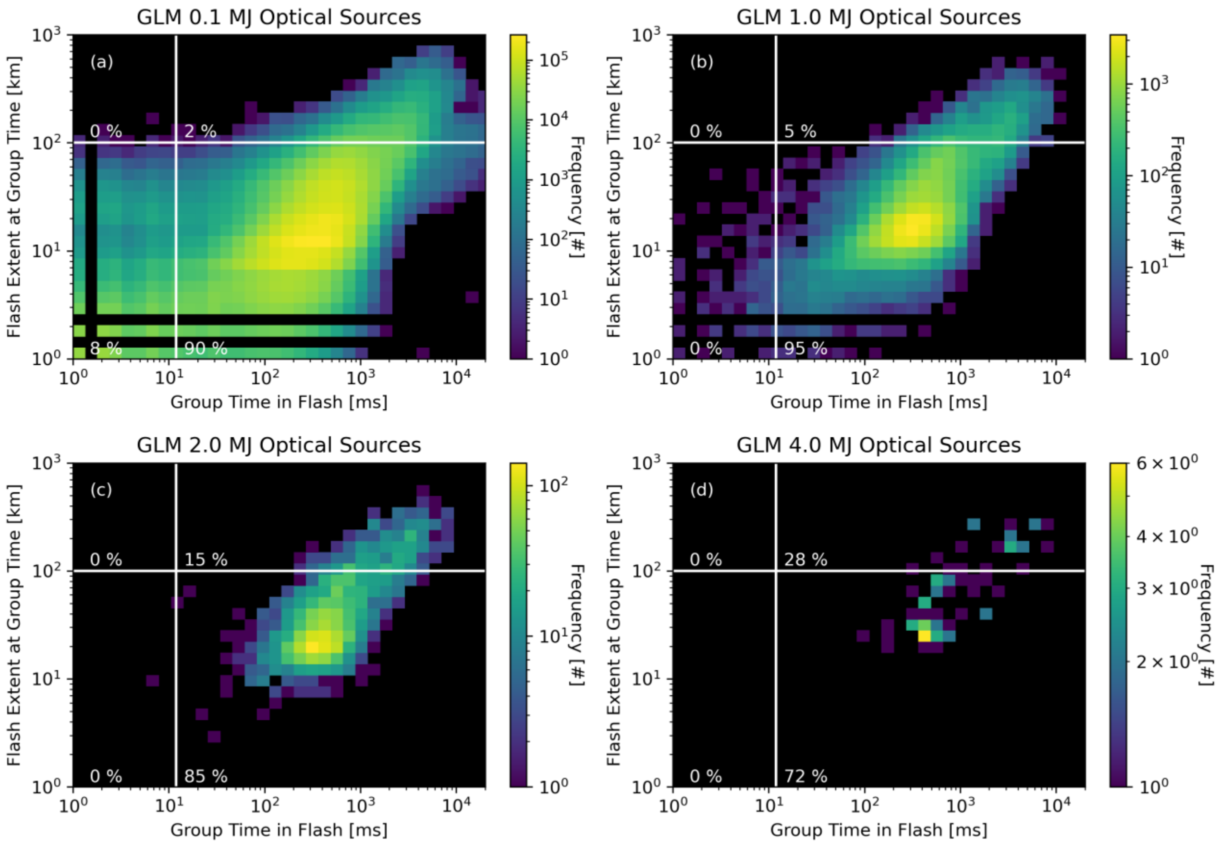

Figure 12. Two-dimensional histograms between the time of the GLM group in its parent flash and the flash extent at the group time for (a) 0.1 MJ optical sources, (b) 1.0 MJ optical sources, (c) 2.0 MJ optical sources, and (d) 4.0 MJ optical sources. Solid lines delineate between prompt and delayed superbolts (vertical line at 12 ms) and flashes that had reached the megaflash scale by the time of the energetic group (horizontal line at 100 km).

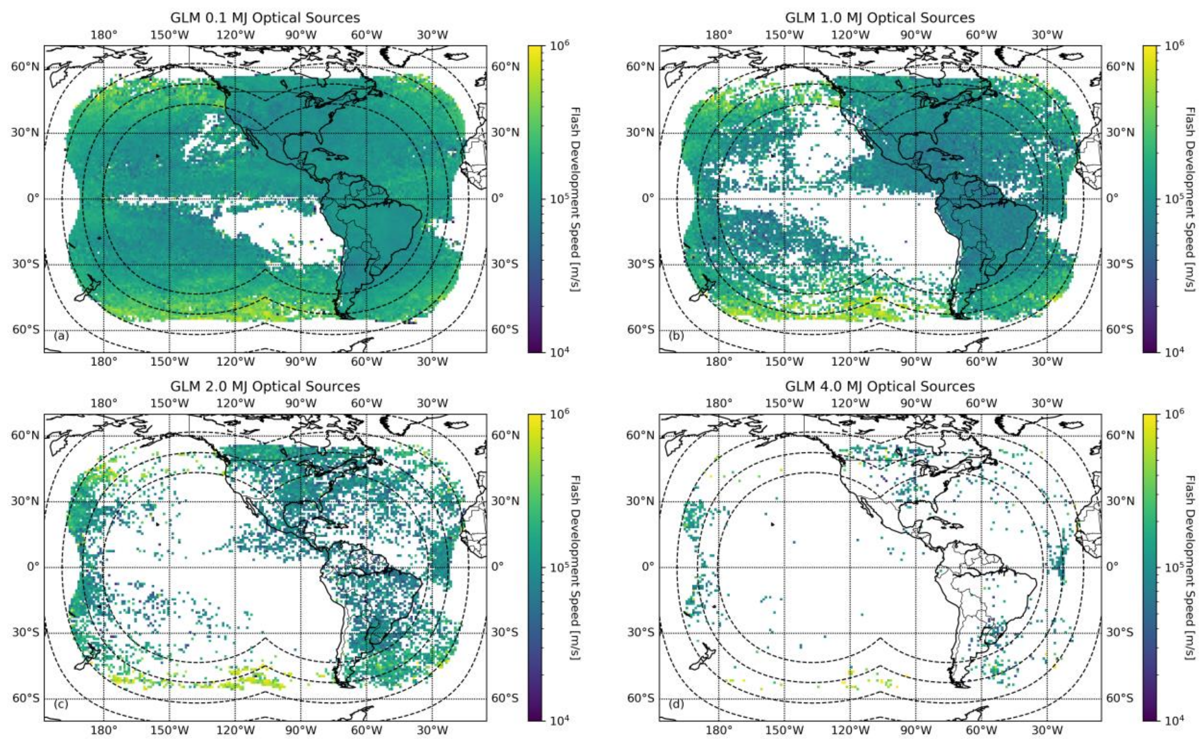

Figure 13. As in Figure 11, but showing the average horizontal development speed of the parent GLM flash.

Figure 1.

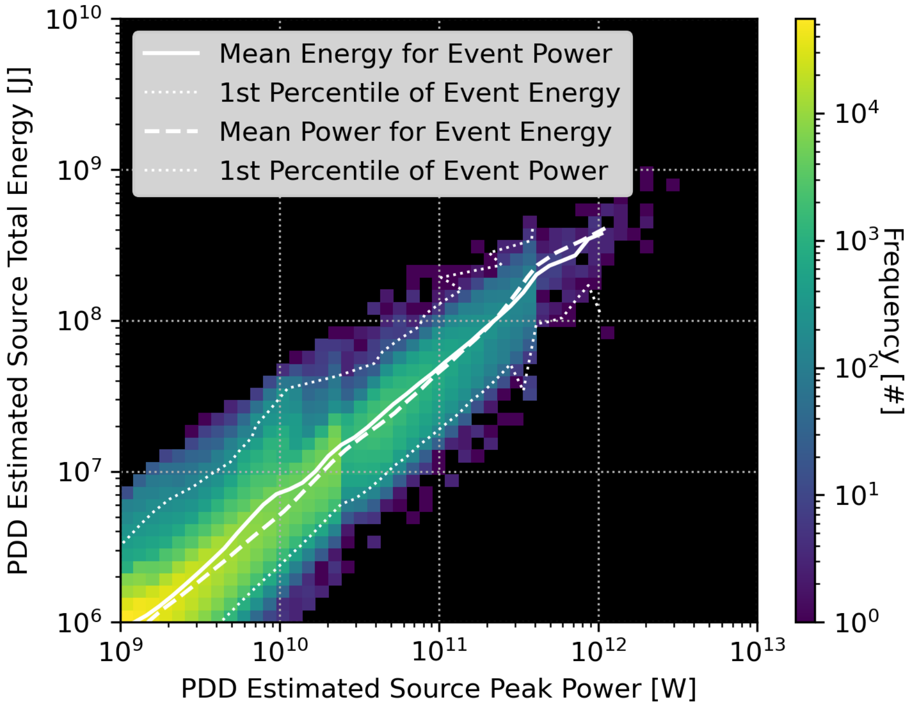

Mean Energy for Event Power
1st Percentile of Event Energy
Mean Power for Event Energy
1st Percentile of Event Power
PDD Estimated Source Total Energy [J]
PDD Estimated Source Peak Power [W]
Frequency [#]
10^{6}
10^{7}
10^{8}
10^{9}
10^{10}
10^{9}
10^{10}
10^{11}
10^{12}
10^{13}
10^{0}
10^{1}
10^{2}
10^{3}
10^{4}

Figure 2.

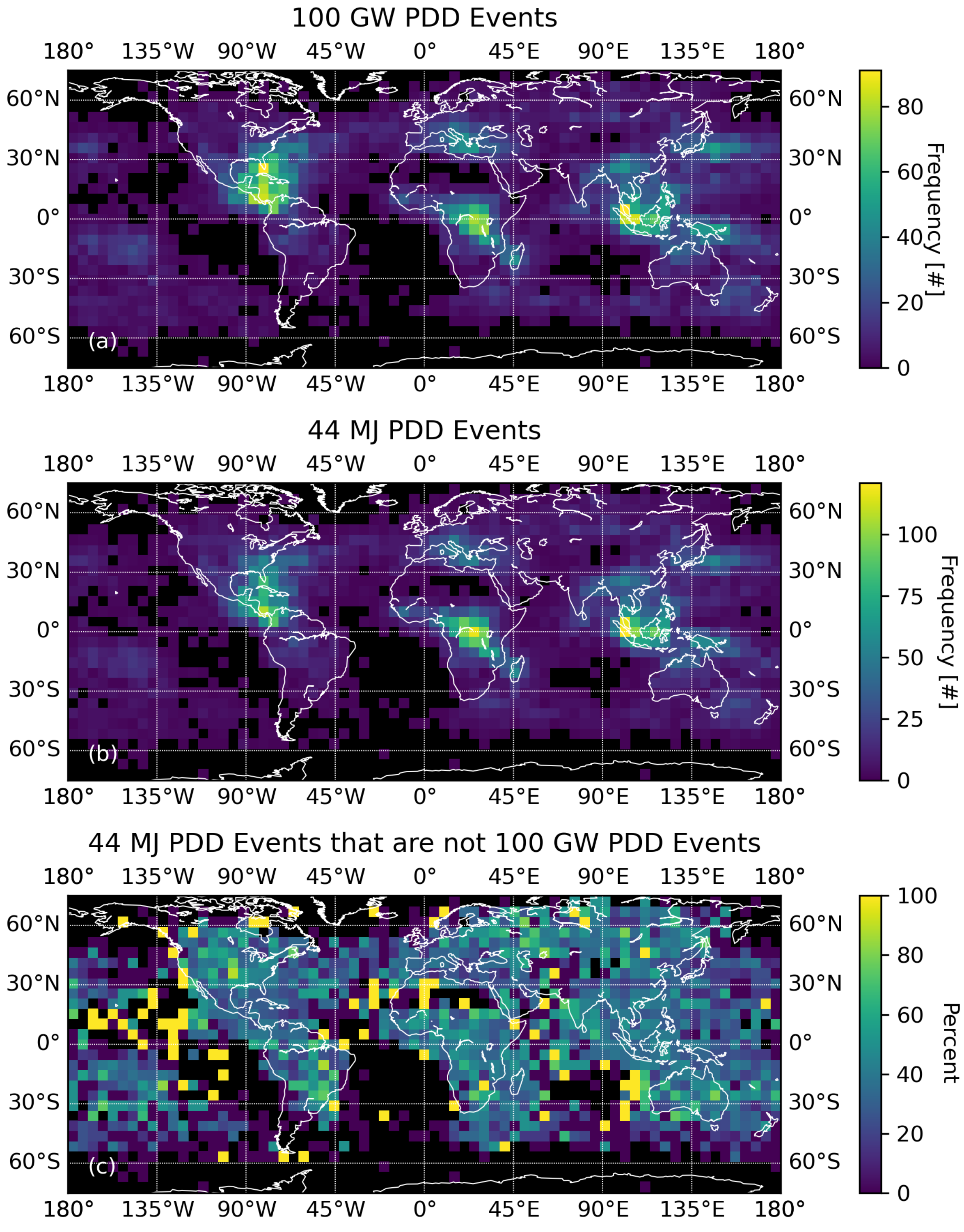
100 GW PDD Events
Frequency [#]
(a)
44 MJ PDD Events
Frequency [#]
(b)
44 MJ PDD Events that are not 100 GW PDD Events
Percent
(c)
180°
135°W
90°W
45°W
0°
45°E
90°E
135°E
60°N
30°N
30°S
60°S

Figure 3.

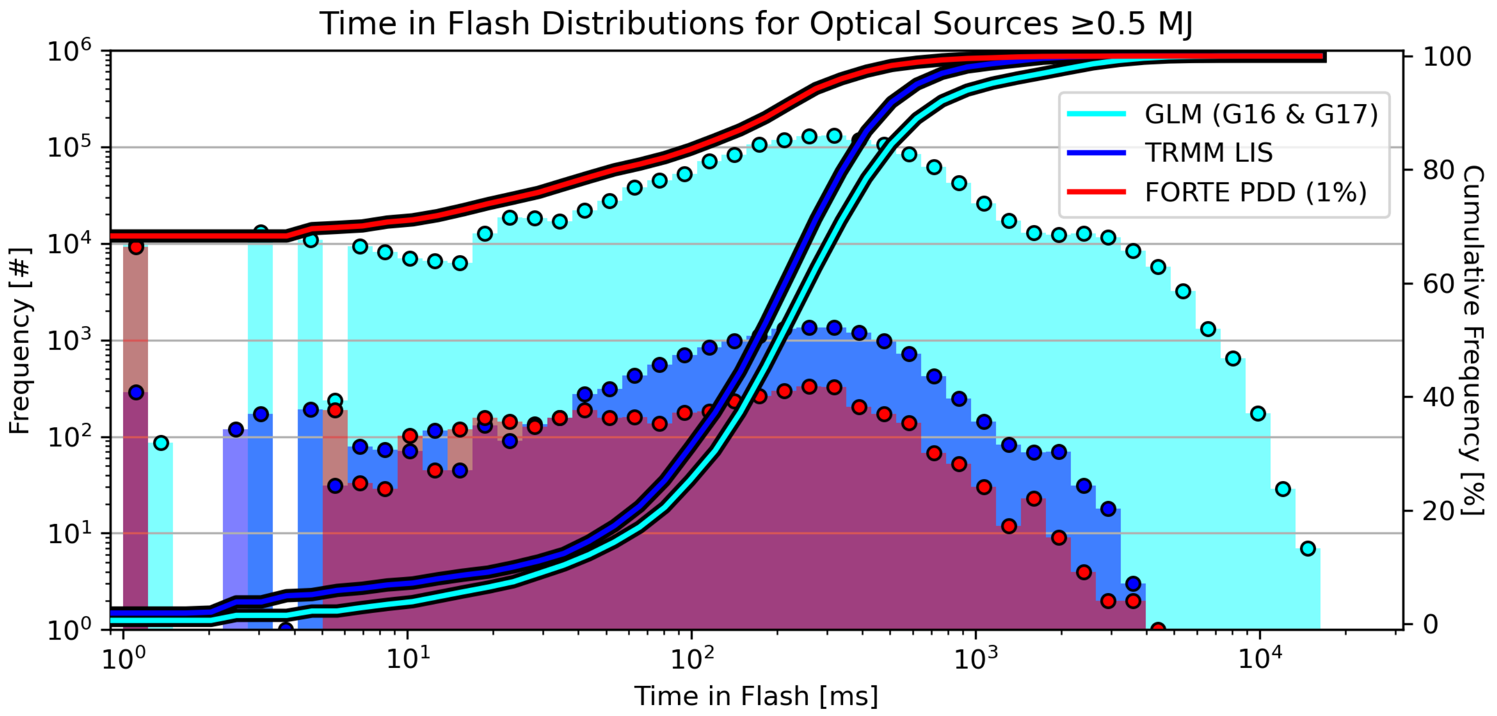

Time in Flash Distributions for Optical Sources ≥0.5 MJ
GLM (G16 & G17)
TRMM LIS
FORTE PDD (1%)
Frequency [#]
Cumulative Frequency [%]
Time in Flash [ms]
10^0
10^1
10^2
10^3
10^4
10^5
10^6
0
20
40
60
80
100

Figure 4.

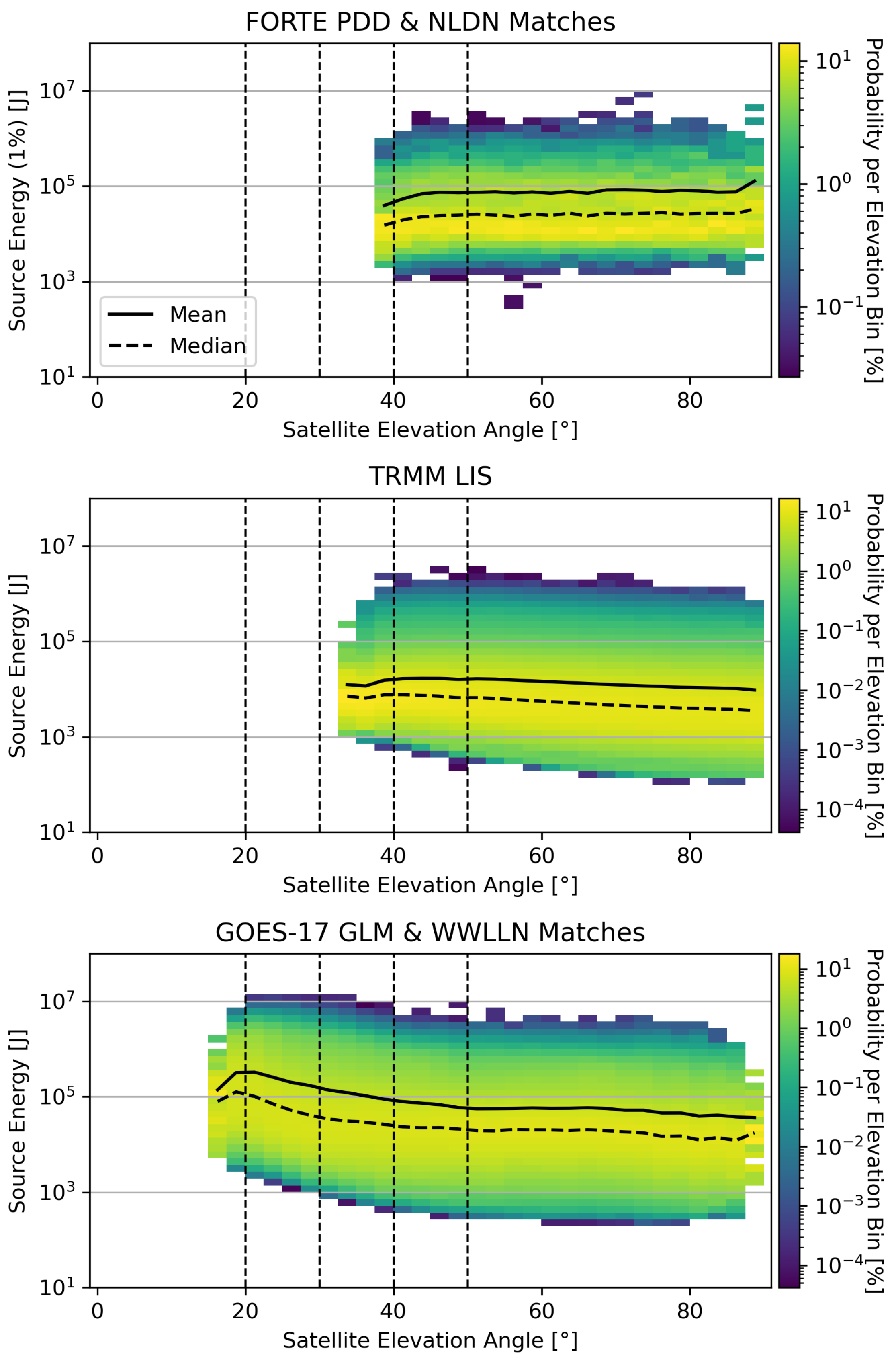

FORTE PDD & NLDN Matches
Source Energy (1%) [J]
Mean
Median
Satellite Elevation Angle [°]
Probability per Elevation Bin [%]
TRMM LIS
Source Energy [J]
Satellite Elevation Angle [°]
Probability per Elevation Bin [%]
GOES-17 GLM & WWLLN Matches
Source Energy [J]
Satellite Elevation Angle [°]
Probability per Elevation Bin [%]

Figure 5.

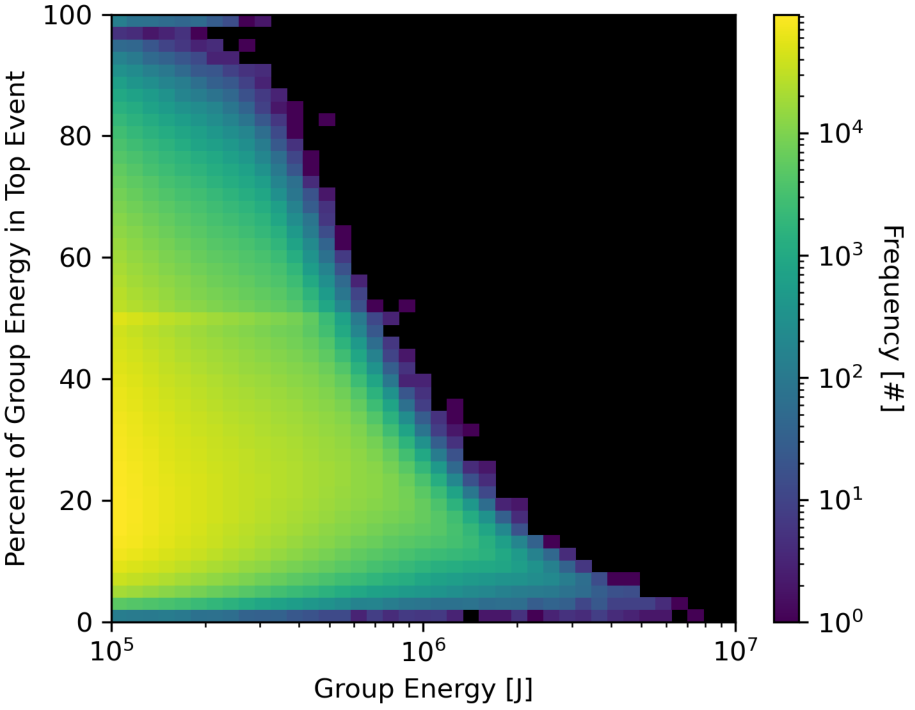

100
80
60
40
20
0
Percent of Group Energy in Top Event
10^5
10^6
10^7
Group Energy [J]
10^4
10^3
10^2
10^1
10^0
Frequency [#]

Figure 6.

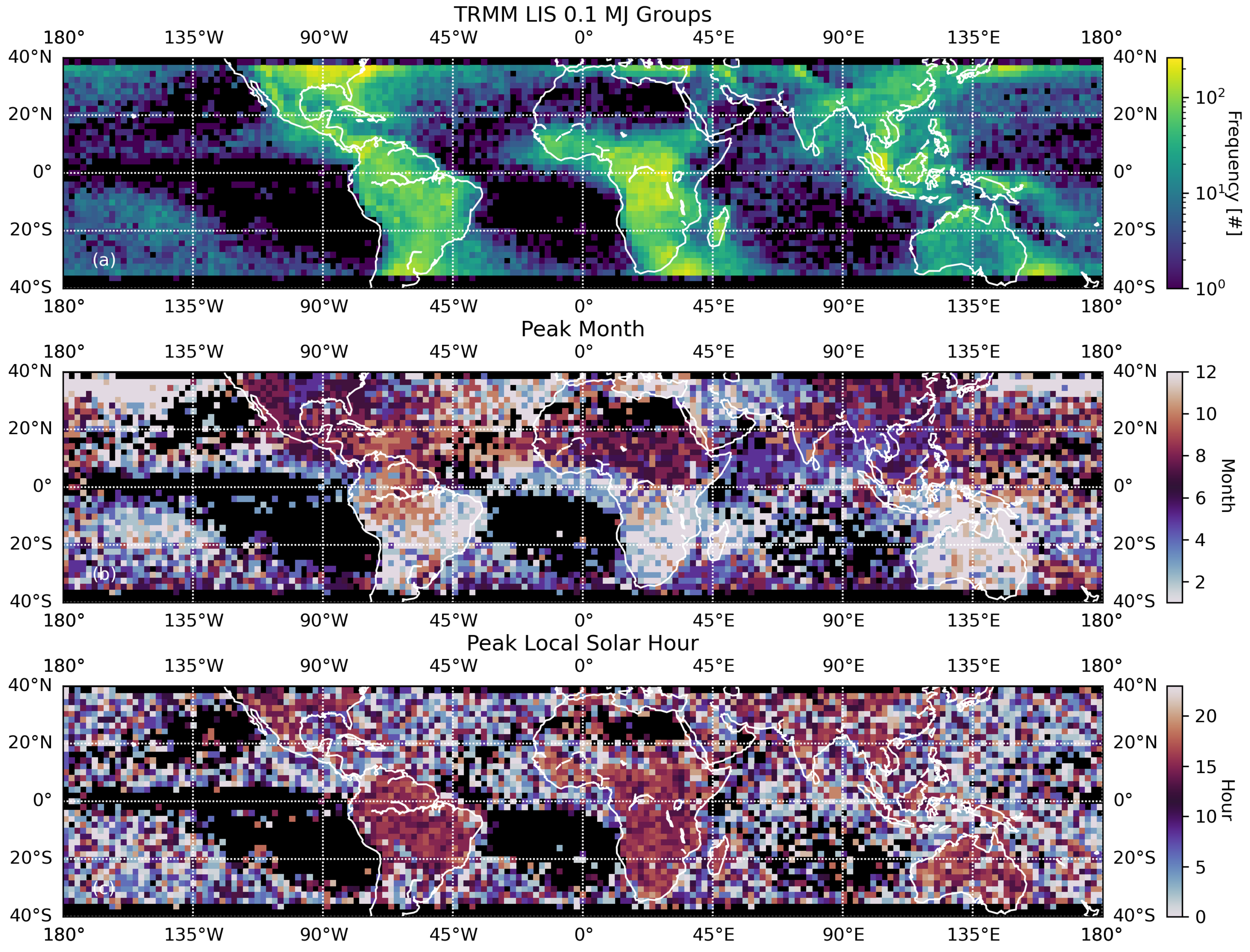

TRMM LIS 0.1 MJ Groups
Peak Month
Peak Local Solar Hour
180°
135°W
90°W
45°W
0°
45°E
90°E
135°E
40°N
20°N
20°S
40°S
(a)
(b)
(c)
Frequency [#]
Month
Hour

Figure 7.

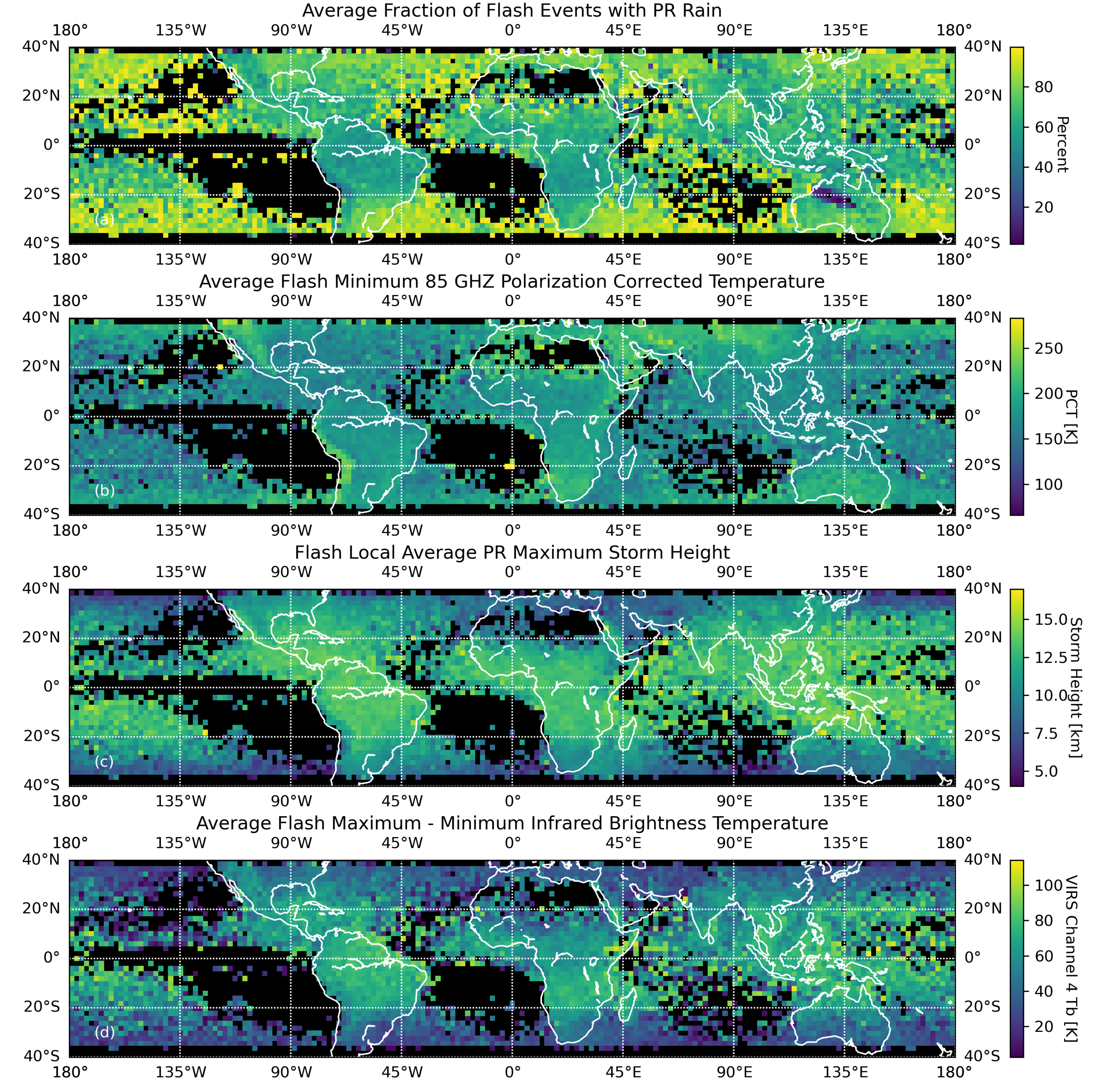
Average Fraction of Flash Events with PR Rain
(a)
Percent
Average Flash Minimum 85 GHZ Polarization Corrected Temperature
(b)
PCT [K]
Flash Local Average PR Maximum Storm Height
(c)
Storm Height [km]
Average Flash Maximum - Minimum Infrared Brightness Temperature
(d)
VIRS Channel 4 Tb [K]
180° 135°W 90°W 45°W 0° 45°E 90°E 135°E 180°
40°N 20°N 0° 20°S 40°S

Figure 8.

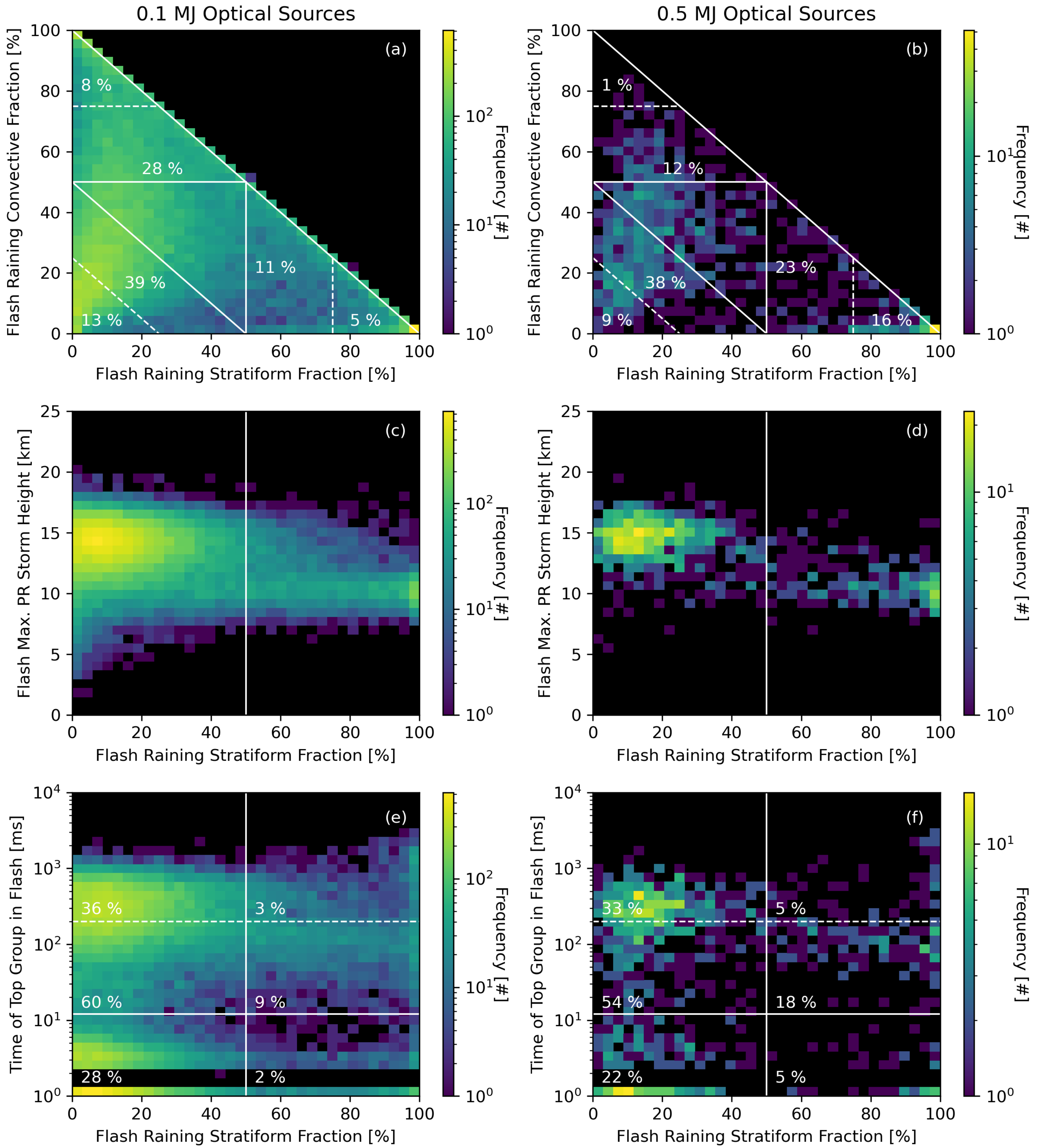

0.1 MJ Optical Sources
0.5 MJ Optical Sources
(a)
(b)
(c)
(d)
(e)
(f)
Flash Raining Convective Fraction [%]
Flash Raining Stratiform Fraction [%]
Flash Max. PR Storm Height [km]
Time of Top Group in Flash [ms]
Frequency [#]
8 %
28 %
39 %
11 %
13 %
5 %
1 %
12 %
38 %
23 %
9 %
16 %
36 %
3 %
60 %
9 %
28 %
2 %
33 %
5 %
54 %
18 %
22 %
5 %

Figure 9.

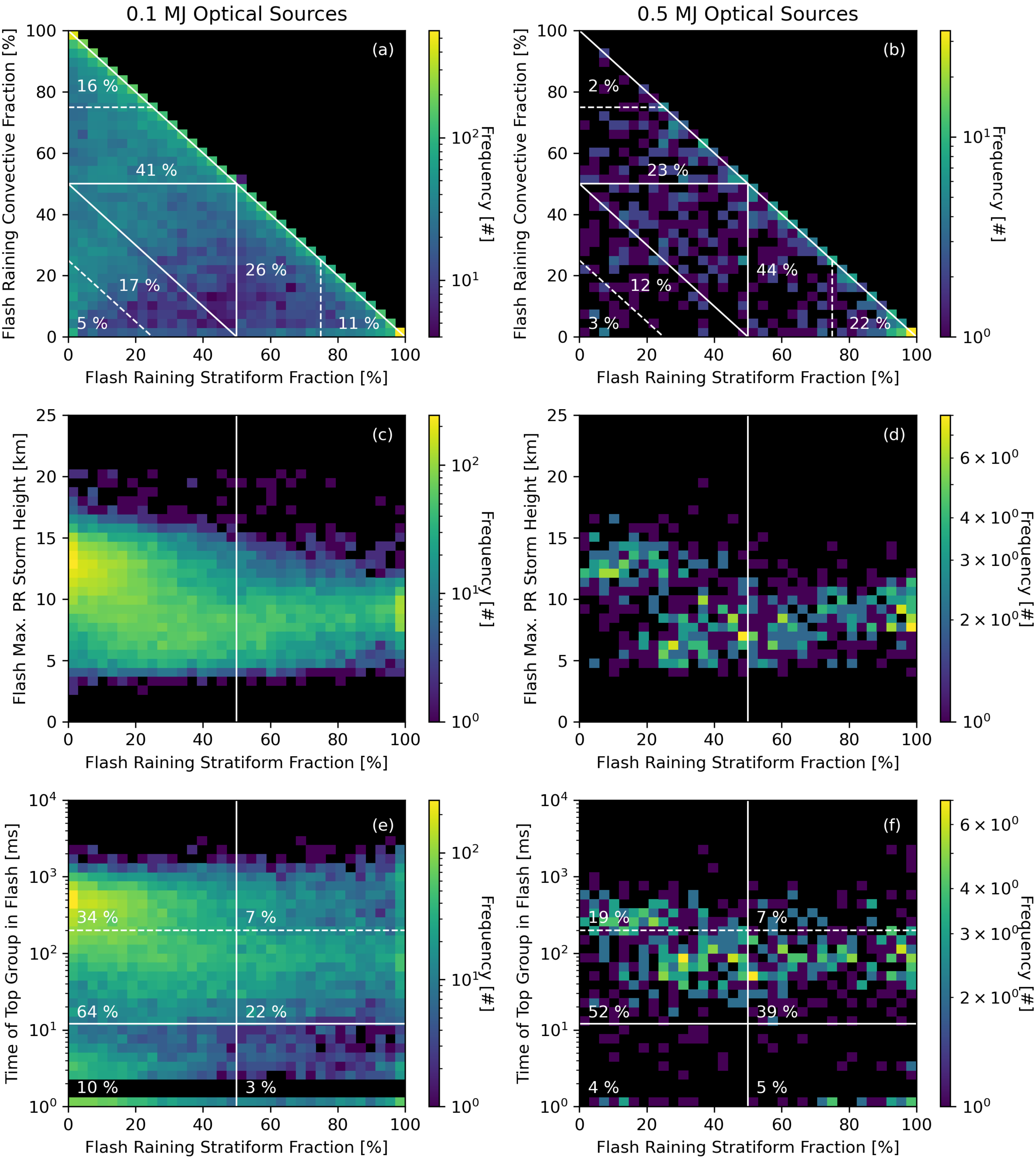
0.1 MJ Optical Sources
0.5 MJ Optical Sources
(a)
(b)
(c)
(d)
(e)
(f)
16 %
41 %
26 %
17 %
5 %
11 %
2 %
23 %
44 %
12 %
3 %
22 %
34 %
7 %
64 %
22 %
10 %
3 %
19 %
7 %
52 %
39 %
4 %
5 %
Flash Raining Convective Fraction [%]
Flash Raining Stratiform Fraction [%]
Flash Max. PR Storm Height [km]
Time of Top Group in Flash [ms]
Frequency [#]

Figure 10.

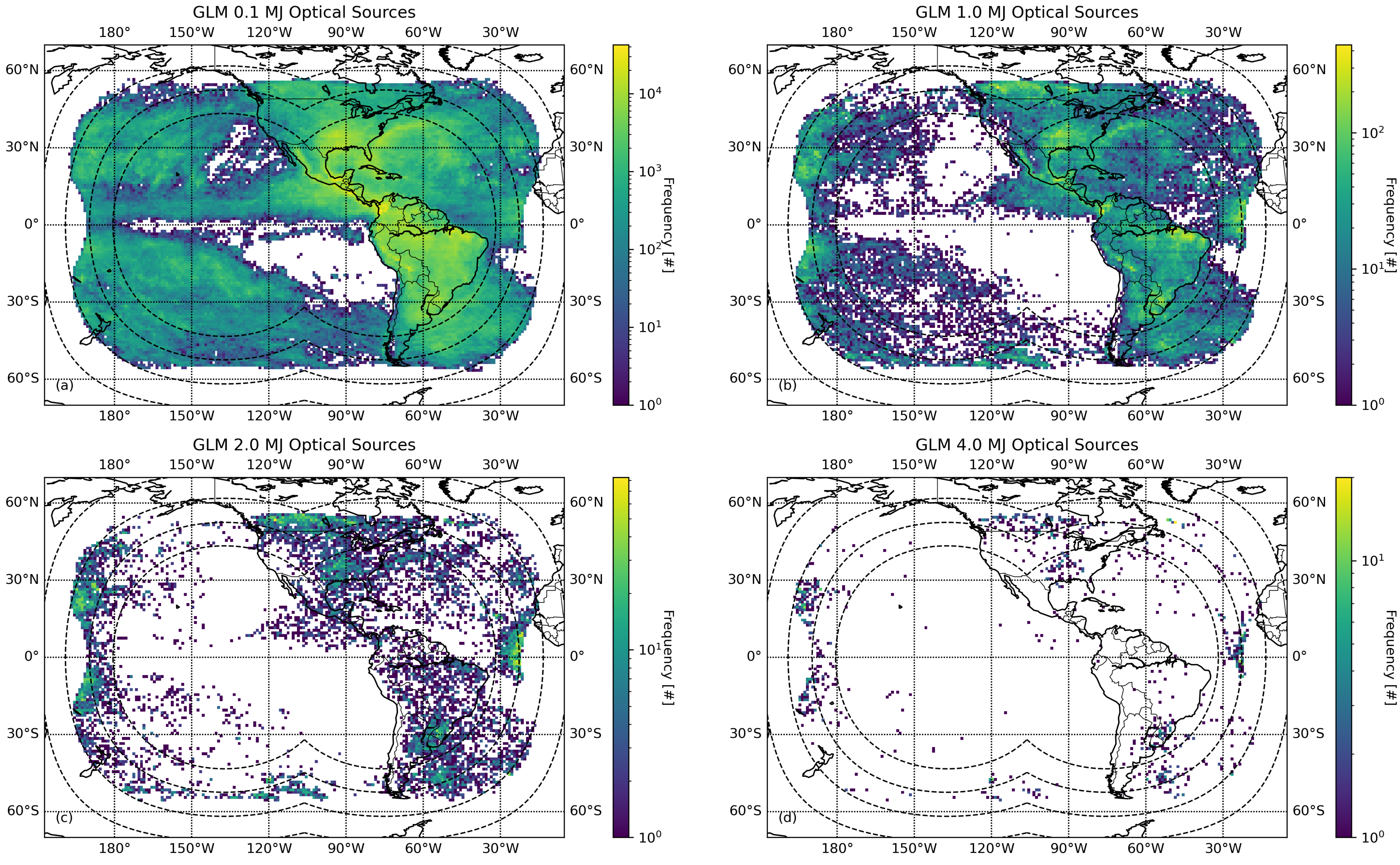
GLM 0.1 MJ Optical Sources
GLM 1.0 MJ Optical Sources
GLM 2.0 MJ Optical Sources
GLM 4.0 MJ Optical Sources
180°
150°W
120°W
90°W
60°W
30°W
60°N
30°N
0°
30°S
60°S
(a)
(b)
(c)
(d)
Frequency [#]
10^0
10^1
10^2
10^3
10^4

Figure 11.

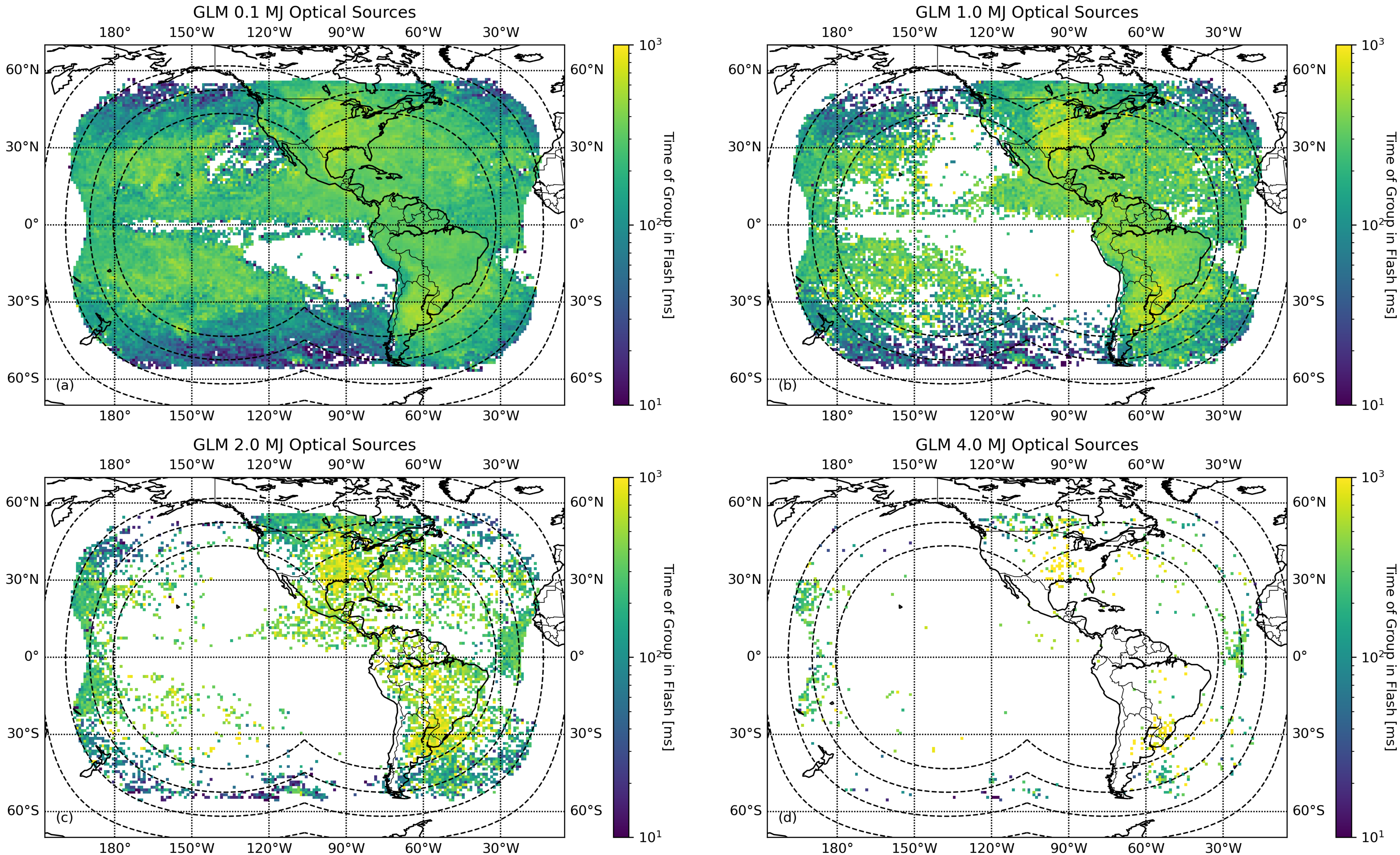

GLM 0.1 MJ Optical Sources
GLM 1.0 MJ Optical Sources
GLM 2.0 MJ Optical Sources
GLM 4.0 MJ Optical Sources
180°
150°W
120°W
90°W
60°W
30°W
60°N
30°N
0°
30°S
60°S
(a)
(b)
(c)
(d)
Time of Group in Flash [ms]
10^3
10^2
10^1

Figure 12.

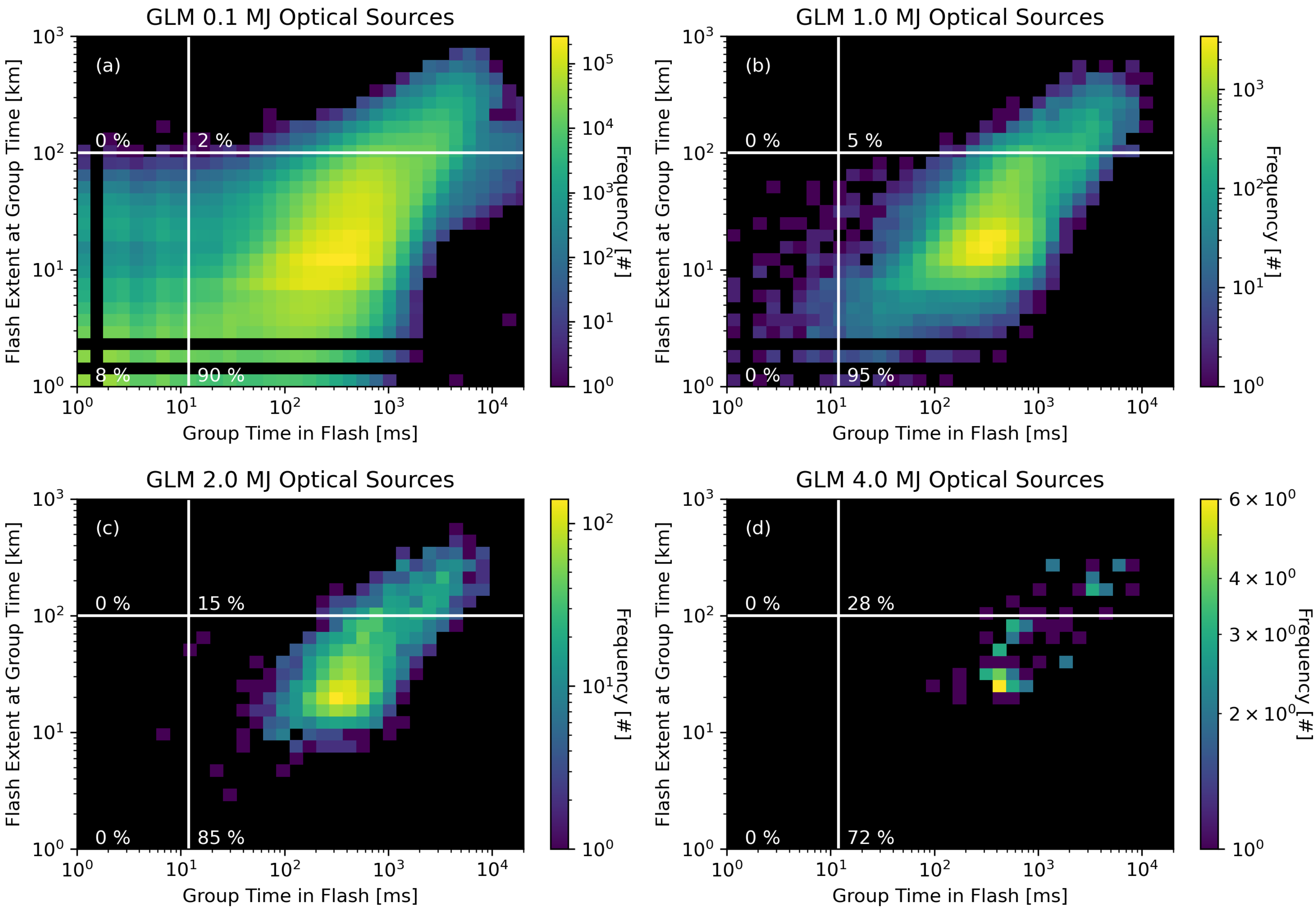

GLM 0.1 MJ Optical Sources
(a)
0 %
2 %
8 %
90 %
Flash Extent at Group Time [km]
Group Time in Flash [ms]
Frequency [#]
GLM 1.0 MJ Optical Sources
(b)
0 %
5 %
0 %
95 %
Flash Extent at Group Time [km]
Group Time in Flash [ms]
Frequency [#]
GLM 2.0 MJ Optical Sources
(c)
0 %
15 %
0 %
85 %
Flash Extent at Group Time [km]
Group Time in Flash [ms]
Frequency [#]
GLM 4.0 MJ Optical Sources
(d)
0 %
28 %
0 %
72 %
Flash Extent at Group Time [km]
Group Time in Flash [ms]
Frequency [#]

Figure 13.

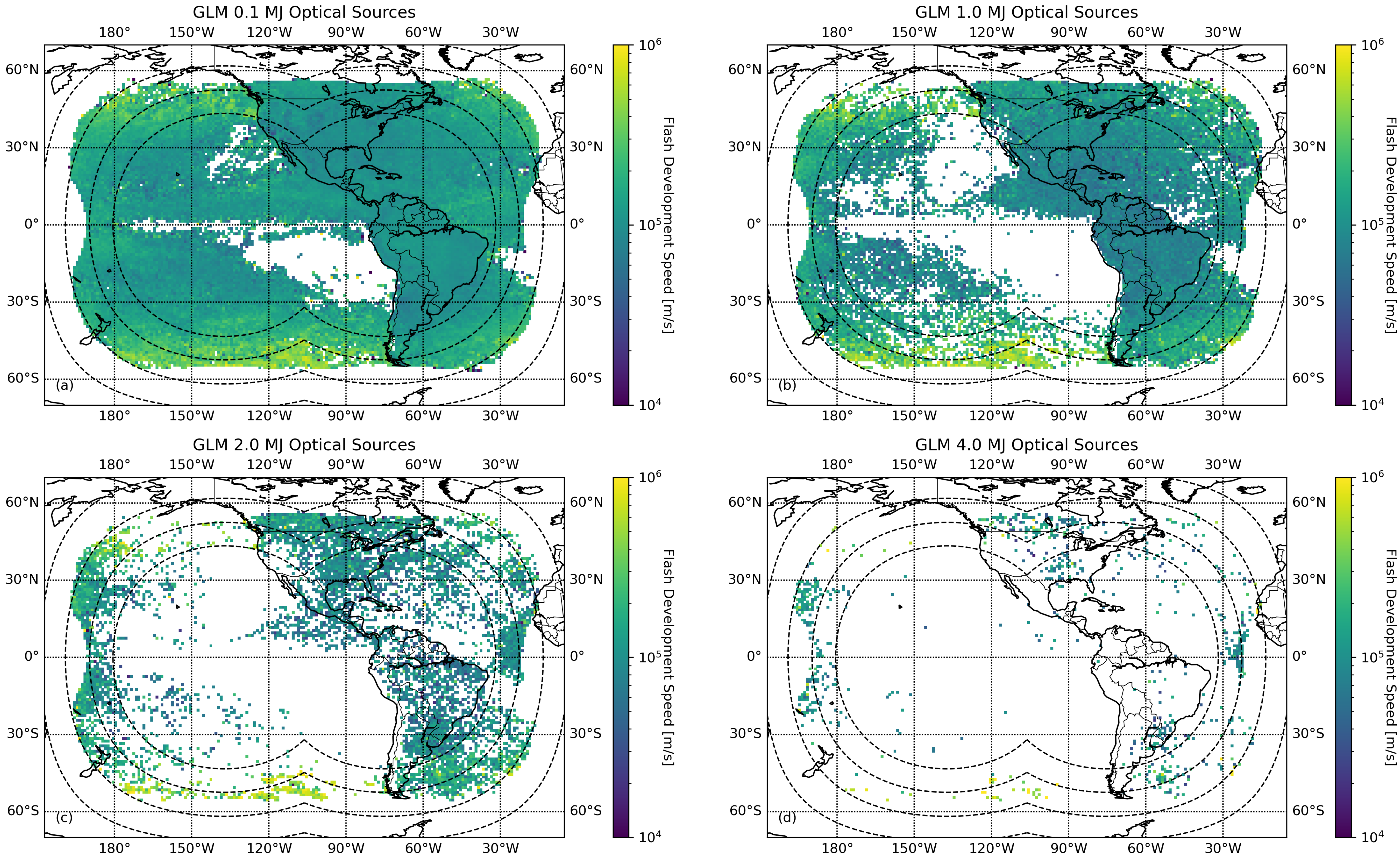
GLM 0.1 MJ Optical Sources
GLM 1.0 MJ Optical Sources
GLM 2.0 MJ Optical Sources
GLM 4.0 MJ Optical Sources
180°
150°W
120°W
90°W
60°W
30°W
60°N
30°N
0°
30°S
60°S
(a)
(b)
(c)
(d)
Flash Development Speed [m/s]
10^4
10^5
10^6